A cross-scale analysis method for lubrication characteristics of micro-textured bearings based on the integration of average flow model and machine learning

Feng, Huihui; Li, Xinyu; Jiang, Shuyun; van Ostayen, Ron; Ji, Taohui

DOI
10.1063/5.0294247

Publication date
2025

Document Version
Final published version

Published in
Physics of Fluids

Citation (APA)
Feng, H., Li, X., Jiang, S., van Ostayen, R., & Ji, T. (2025). A cross-scale analysis method for lubrication characteristics of micro-textured bearings based on the integration of average flow model and machine learning. *Physics of Fluids*, *37*(10), Article 103613. https://doi.org/10.1063/5.0294247

RESEARCH ARTICLE | OCTOBER 13 2025

A cross-scale analysis method for lubrication characteristics of micro-textured bearings based on the integration of average flow model and machine learning

Huihui Feng ; Xinyu Li; Shuyun Jiang; Ron van Ostayen ; Taohui Ji

Physics of Fluids 37, 103613 (2025)
https://doi.org/10.1063/5.0294247

Physics of Fluids ARTICLE pubs.aip.org/aip/pof

A cross-scale analysis method for lubrication characteristics of micro-textured bearings based on the integration of average flow model and machine learning

Cite as: Phys. Fluids **37**, 103613 (2025); doi: 10.1063/5.0294247
Submitted: 2 August 2025 · Accepted: 25 September 2025 ·
Published Online: 13 October 2025

View Online Export Citation CrossMark

Huihui Feng,[1,a)] Xinyu Li,[1] Shuyun Jiang,[2] Ron van Ostayen,[3] and Taohui Ji[1]

AFFILIATIONS

[1]College of Mechanical and Electrical Engineering, Hohai University, Changzhou, Jiangsu 213022, People's Republic of China
[2]School of Mechanical Engineering, Southeast University, Jiangning District, Nanjing, Jiangsu 211189, People's Republic of China
[3]Department of Precision and Microsystems Engineering, Delft University of Technology, 2628 CD Delft, The Netherlands

[a)]**Author to whom correspondence should be addressed:** fenghh@hhu.edu.cn

ABSTRACT

Micro-textured water-lubricated thrust bearings exhibit significant potential in motorized spindles due to their low friction, high heat dissipation efficiency, and superior damping performance. However, existing numerical methods for evaluating the lubrication performance of such bearings face challenges in balancing computational efficiency with accuracy, along with limitations in macro-micro cross-scale coupling capabilities. To address these issues, this study proposes a novel approach combining the flow factor model with a machine learning algorithm. First, the average Reynolds equation based on the average flow model (AF-ARE) is formulated using flow factors. However, results indicate that when dealing with high-density textures with small diameters, AF-ARE still suffers from computational inefficiency as it requires individual calculation of flow factors for each texture element. To address this limitation, machine learning-based prediction models are subsequently developed using three algorithms: Gaussian process regression, support vector machine, and extreme learning machine. The prediction models enable rapid estimation of flow factors for all texture elements, and their predictive performances are systematically compared and evaluated. Subsequently, by integrating these flow factor prediction models with the average Reynolds equation, a novel average flow-machine learning-averaged Reynolds equation (AFML-ARE) method is proposed. The proposed AFML-ARE multiscale numerical method offers a novel approach to overcome current research limitations in cross-scale numerical analysis of lubrication characteristics for high-density, small-diameter micro-textured bearings, enabling efficient performance evaluation from microscopic texture effects to macroscopic bearing behavior.

I. INTRODUCTION

The use of water-lubricated bearings has become a promising direction for high-precision motorized spindle due to their environmental friendliness, low friction, and good damping.[1] In recent years, researchers have explored the application of surface textures on water-lubricated bearing surfaces to further enhance their load-carrying capacity.[2] Studies have shown that appropriately designed surface textures can effectively improve both frictional performance and load capacity.[3–6]

When numerically solving micro-textured fluid bearings, one key challenge is the significant scale difference between the macroscopic dimensions of the bearing and the microscopic dimensions of the surface textures, as illustrated in Fig. 1. Currently, two main approaches are used to numerically solve the performance of the textured bearings: the direct method and the indirect method.

In the direct method, the mesh is refined sufficiently to capture the microscopic features of the surface texture, incorporating the texture effects directly into the film thickness calculation. Currently, the majority of the research on textured fluid bearings employ this direct approach. The Reynolds equation[7–11] or the Navier–Stokes equations,[12–14] often considering cavitation, are numerically solved to analyze the influences of the parameters of surface textures and operating

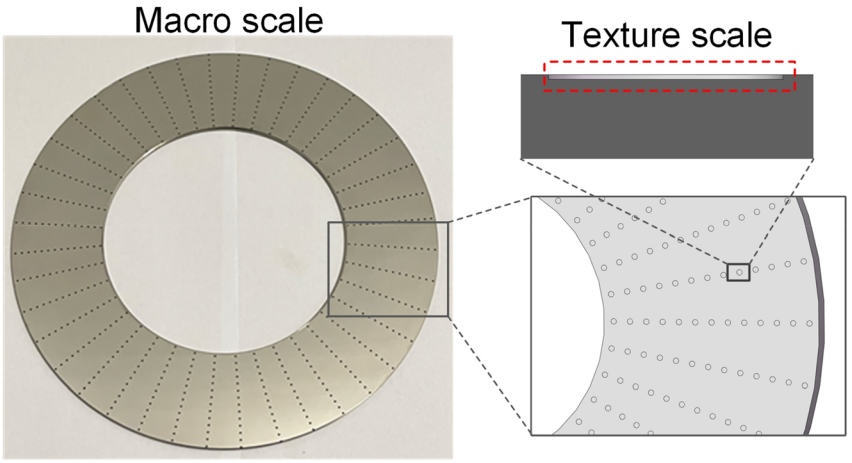

FIG. 1. Schematic of the cross-scale problem in textured thrust bearings. The large gap between macro bearing size and micro texture size illustrates the challenge of direct discretization.

conditions of bearings on the pressure distribution and load capacity of bearings. However, there exist a critical conflict between mesh resolution and computational efficiency: when dealing with bearing with high density textures or micro-scale textures, whether using traditional finite volume methods or numerical solutions of the Reynolds equation, micro-scale (micron-level) meshes are required in the textured regions. This leads to an extremely large global mesh count—on the order of hundreds of millions[15] (for example, the 2D mesh count for a 50 mm diameter bearing exceeds 10^8)—leading to computational costs to increase dramatically.

To address the numerically solving challenges of cross-scale effects on textured bearing surfaces, some researchers have introduced statistical methods that have been originally developed for the investigation of rough surfaces considering roughness into the performance analysis of textured bearings, indirectly characterizing surface textures due to the similarity in scale between surface roughness and micro-textures.[6,16] Currently, two main indirect methods are widely used: the average flow model and the homogenization method. De Kraker *et al.*[17] extended the average flow model proposed by Patir and Cheng, which describes surface roughness, to study the performance of individual texture units by introducing pressure flow factors and shear flow factors. Their work treats surface textures as a special form of roughness and formulates a modified Reynolds equation that accounts for texture effects, providing a theoretical basis for analyzing the lubrication performance of textured bearings. Waseem *et al.*[18] carried out optimal design of micro-textures on hydrodynamic lubrication surfaces based on homogenization theory. This method establishes a multi-scale coupling model that combines microscopic texture features with macroscopic lubrication performance, enabling the optimized design of texture parameters. Rom and Müller[19] pointed out that the statistical coefficients of micro-texture cells depend on variations in the macroscopic film thickness. Therefore, solving textured bearings requires calculating a large number of texture unit coefficients. To speed up this process, they proposed a simplification method to compute homogenized coefficients for all textures. These studies demonstrate that indirect methods are effective for solving textured bearing problems and provide important theoretical support and practical approaches for analyzing the lubrication performance of textured bearings.

In recent years, with the rapid speed development of machine learning (ML) techniques, they are gradually used to study the frictional and wear performance of bearings. Researchers primarily use ML methods, such as regression trees (RT), artificial neural networks (ANN), ensemble boosting trees (EBT), and random forests (RF), to predict bearing friction and wear performance based on the experimental data.[20–25] Results demonstrate that machine learning algorithms can effectively predict friction and wear behaviors of bearings.

Despite the progress of both direct and indirect numerical methods, current research still faces several critical limitations when analyzing micro-textured bearings, especially under high texture density and small feature scales. Most existing indirect methods either rely on fixed flow factors or oversimplified homogenization assumptions, failing to dynamically reflect the mutual coupling between local texture effects and global bearing behavior. In addition, when texture parameters vary, current models require repeated re-computation of numerous micro-scale coefficients, which severely limits the efficiency of optimization and large-scale parametric studies. Furthermore, while machine learning has shown promise in predicting bearing performance, its potential in cross-scale lubrication modeling remains under explored. Therefore, it is necessary to propose an efficient and adaptive method that can both capture the complex multi-scale interactions and reduce the computational consumption associated with high-density micro-textures.

Considering the advantages and limitations of machine learning algorithms as well as the scale characteristics of micro-textured hydrodynamic bearings, this study proposes a hybrid approach that integrates data-driven machine learning algorithms with the average flow Reynolds model to study the lubrication performance of micro-textured bearings. First, a mathematical model of the average Reynolds equation (AF-ARE model) based on the average flow model is presented, introducing flow factors for low density textured bearing. Next, to address the high computational cost and low analysis efficiency caused by the bearings with large density and micro-textures, a novel method integrating machine learning algorithms to establish flow factor prediction models is proposed. Then, by coupling the flow factor prediction models with the average Reynolds equation, an average Reynolds equation model integrating machine learning algorithm, and the average flow model (AFML-ARE model) is established.

The computational efficiency, pressure distribution, and load capacity of high density, micro-textured bearings obtained using the proposed AFML-ARE method are analyzed and compared with those from the traditional direct numerical solving method based on Reynolds equation (RE model). Finally, test rigs are manufactured and experimental investigation of lubrication behavior of textured thrust bearings are conducted to validate the theoretical results through comparison with experimental data.

By using machine learning to predict the dynamic flow factors of individual textures efficiently, this method could avoid the need for large-scale computations of flow factors and addresses the challenge of capturing micro-macro coupling effects.

The graphical framework of the proposed AFML-ARE method is illustrated in Fig. 2 and the overall process flow chart is illustrated in Fig. 3.

II. AVERAGE FLOW REYNOLDS MODEL

In this work, to solve the pressure distribution of textured water-lubricated thrust bearing, the average flow Reynolds model proposed by Patir and Cheng[26] is adopted and further improved. The flow factors including pressure flow factors and shear flow factors for a base area with a circular texture are derived first and then the Reynolds equation combined with average flow model is presented.

A. Deduction of flow factors (microscale)

Consider a control volume with base area L_{cellx}·L_{celly}, as shown in Fig. 4. A circular micro texture with depth of h_d is included by the base area. The unit flow in the x and y directions are given as follows:

$$q_x = -\frac{h^3}{12\mu}\frac{\partial p}{\partial x} + \frac{U}{2}h, \qquad q_y = -\frac{h^3}{12\mu}\frac{\partial p}{\partial y}, \tag{1}$$

where h is the film thickness, μ is the viscosity of fluid, p is the pressure, and U is the velocity. The flow can be classified into two types: the Poiseuille flow and Couette flow along x and y directions. According to the principle that the flow rate into a control unit with micro-texture equals the flow rate into a equivalent smooth control volume, the flow rate into the control unit with micro-texture can be equivalently represented as the flow rate into a smooth control unit with a nominal film thickness.

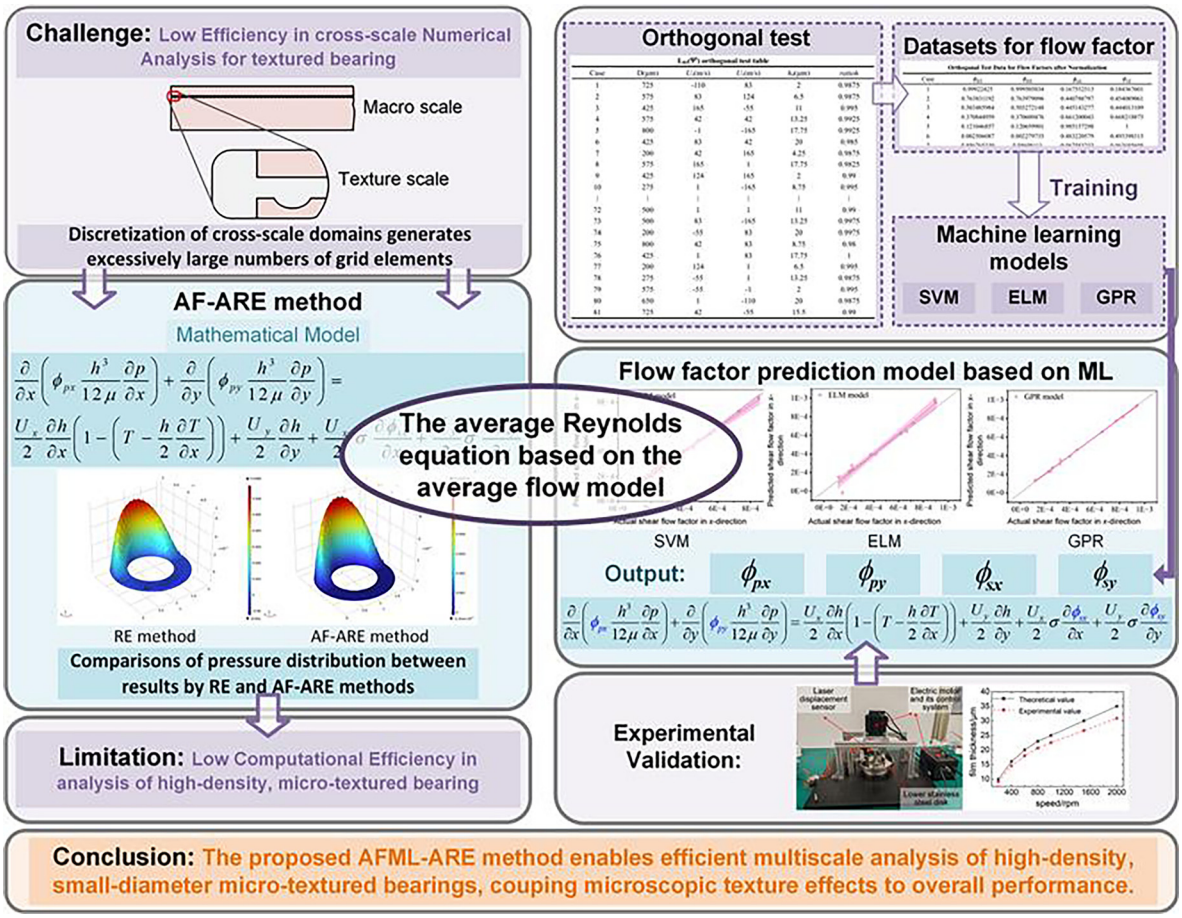

FIG. 2. Graphical framework of the proposed AFML-ARE method. The framework combines AF-ARE modeling with machine-learning-based flow factors and validation.

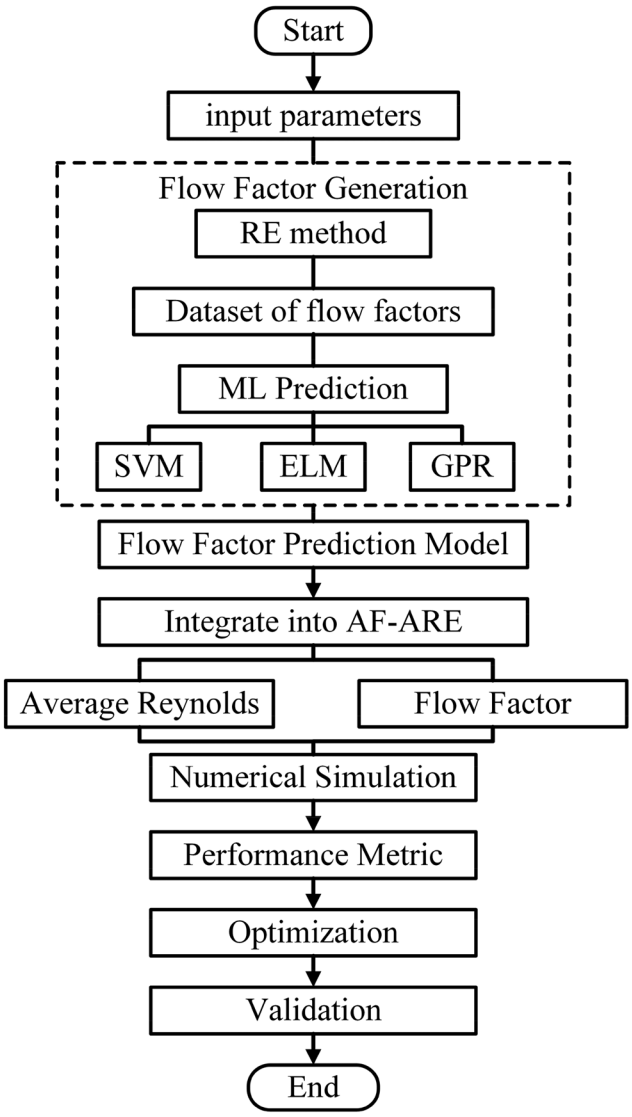

FIG. 3. Overall process flowchart.

Accordingly, the coefficients derived from the pure pressure-driven flow, namely, Poiseuille flow are referred to as pressure flow factors, while those derived from the pure shear-driven flow, namely, Couette flow are referred to as shear flow factors.

For each textured bearing, the flow rate into the equivalent smooth unit can be calculated by defining a nominal film thickness. For bearing units with different nominal film thicknesses, the flow factors are functions of the film thickness h. As shown in Fig. 5, the nominal film thickness h_{nom} is defined as the distance between the centerline of the texture and the bush surface.

The pressure-driven flow in the x-direction is shown in Fig. 6. For the Poiseuille flow, the Reynolds equation is expressed as

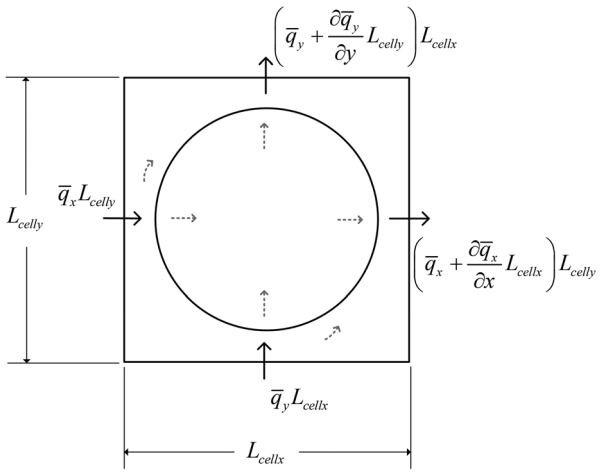

FIG. 4. Control volume for flow factor derivation. A unit cell with a circular texture is used to compute pressure- and shear-driven flows.

$$\frac{\partial}{\partial x}\left(\frac{h^3}{12\mu}\frac{\partial p}{\partial x}\right) + \frac{\partial}{\partial y}\left(\frac{h^3}{12\mu}\frac{\partial p}{\partial y}\right) = 0, \tag{2}$$

where the flow rate per unit width in the x-direction is given by the following equation:

$$q_x = -\frac{h^3}{12\mu}\frac{\partial p}{\partial x} = -\frac{c^3 P_0}{12\mu_0 L_{cellx}}\frac{\overline{H}^3}{\overline{\mu}}\frac{\partial \overline{P}}{\partial \overline{X}} \tag{3}$$

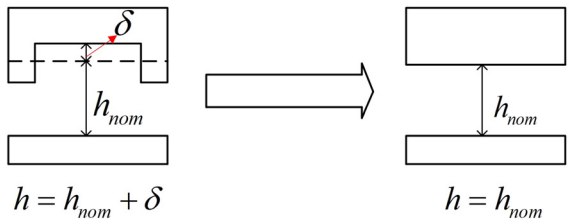

FIG. 5. Presentation of nominal film thickness.

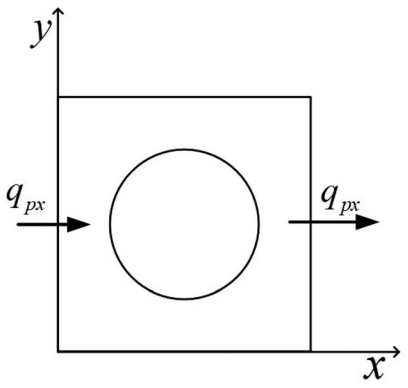

FIG. 6. Pressure-driven flow in the x-direction.

where $h = c\overline{H}$, $p = P_0\overline{P}$, $\mu = \mu_0\overline{\mu}$, $x = L_{cellx}\overline{X}$, $P_0 = \mu_0 U_0 L/c^2$, c represents the film thickness at the maximum clearance of the thrust pad, and p_0 represents the reference pressure. In this equation, μ_0 is the dynamic viscosity of water, U_0 is the characteristic velocity, and L is the outer radius of the thrust pad.

Then, the average unit flow rate exiting the control volume is expressed as

$$\overline{q_{xt}} = \frac{1}{L_{celly}} \int_0^{L_{celly}} q_x dy. \tag{4}$$

Assuming the unit flow rate exits the equivalent smooth control volume with a nominal film thickness h_{nom}, and defining the pressure flow factor ϕ_{px}, the average unit flow rate exiting the equivalent smooth control volume is given by

$$\overline{q_{xs}} = -\frac{c^3 P_0}{12\mu_0 L_{cellx}} \frac{\phi_{px} H_{nom}^3}{\overline{\mu}} \frac{\partial \overline{P}}{\partial \overline{X}}. \tag{5}$$

Driven by Poiseuille flow in the x-direction, the average unit flow rate of the smooth control unit is uniform along the y-direction; therefore, Eq. (5) can be equivalently expressed as

$$\overline{q_{xs}} = -\frac{c^3 P_0}{12\mu_0 L_{cellx}} \frac{\phi_{px} H_{nom}^3}{\overline{\mu}} \frac{\Delta \overline{P}}{\Delta \overline{X}}. \tag{6}$$

Substituting Eq. (3) into Eq. (4) and according to the equality of flow rates through the textured control unit and the equivalent smooth control unit, the pressure flow factor can be obtained as

$$\phi_{px} = \frac{\overline{\mu}\Delta\overline{X}}{H_{nom}^3 \Delta\overline{P}} \int_0^{L_{celly}} \frac{\overline{H}^3}{\overline{\mu}} \frac{\partial \overline{P}}{\partial \overline{X}} d\overline{Y}. \tag{7}$$

From Eq. (7), it can be seen that the pressure flow factor can be calculated by applying an arbitrary pressure gradient $\Delta\overline{P}/\Delta\overline{X}$ at the boundary. For computational convenience, let $\Delta\overline{P}/\Delta\overline{X} = -1$; since viscosity variations are not considered here, $\overline{\mu} = 1$; the pressure flow factor in the x-direction is given by

$$\phi_{px} = -\frac{1}{H_{nom}^3} \int_0^{L_{celly}} \overline{H}^3 \frac{\partial \overline{P}}{\partial \overline{X}} d\overline{Y}. \tag{8}$$

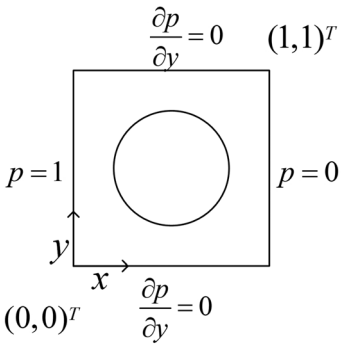

FIG. 7. Boundary conditions for calculating the pressure flow factor in the x-direction. A unit pressure gradient is applied along x-direction.

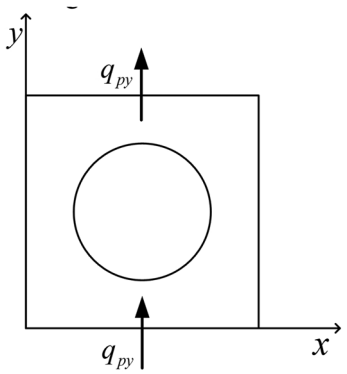

FIG. 8. Pressure-driven flow in the y-direction used to calculate the pressure flow factor ϕ_{py}.

Since only the pressure-driven flow along the x-direction is considered here, the other two boundaries of the control unit are set to $\partial p/\partial y = 0$.[16,26] The boundary conditions are illustrated in Fig. 7.

Similarly, the pressure-driven flow along the y-direction is shown in Fig. 8, with boundary conditions illustrated in Fig. 9. Using the same approach, the pressure flow factor in the y-direction is derived as

$$\phi_{py} = -\frac{1}{H_{nom}^3} \int_0^{L_{cellx}} \overline{H}^3 \frac{\partial \overline{P}}{\partial \overline{Y}} d\overline{X}. \tag{9}$$

For the Couette flow, the Reynolds equation is as follows:

$$\frac{\partial}{\partial x}\left(\frac{h^3}{12\mu}\frac{\partial p}{\partial x}\right) + \frac{\partial}{\partial y}\left(\frac{h^3}{12\mu}\frac{\partial p}{\partial y}\right) = \frac{U_x}{2}\frac{\partial h}{\partial x} + \frac{U_y}{2}\frac{\partial h}{\partial y}. \tag{10}$$

The shear flow factors can be calculated by applying an arbitrary pressure gradient at the boundaries. Since the fluid under pure shear flow is not influenced by pressure-driven flow, the pressure boundary conditions are as shown in Fig. 10.[16]

Similarly, the shear flow factors ϕ_{sx} and ϕ_{sy} are derived as follows:[16]

$$\phi_{sx} = \frac{1}{6\overline{U_x}\overline{\sigma}} \int_0^{L_{celly}} \left(-\frac{\overline{H}^3}{\overline{\mu}} \frac{\partial \overline{P}}{\partial \overline{X}}\right) d\overline{Y}, \tag{11}$$

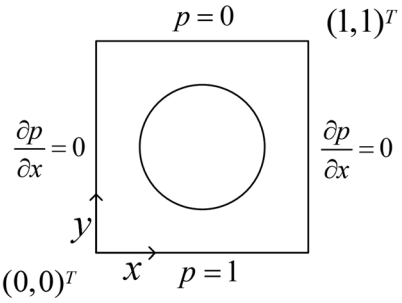

FIG. 9. Boundary conditions for calculating the pressure flow factor in the y-direction. A unit pressure gradient is imposed along y-direction.

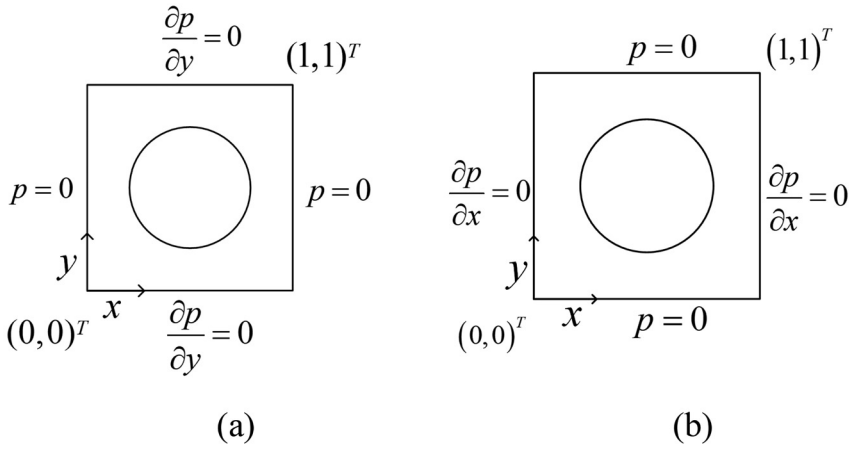

FIG. 10. Boundary conditions for calculating the shear flow factor. (a) Boundary conditions for calculating the shear flow factor in the *x*-direction and (b) boundary conditions for calculating the shear flow factor in the *y*-direction.

$$\phi_{sy}=\frac{1}{6\overline{U}_y\overline{\sigma}}\int_0^{L_{cells}}\left(-\frac{\overline{H}^3}{\overline{\mu}}\frac{\partial\overline{P}}{\partial\overline{Y}}\right)d\overline{X}, \tag{12}$$

where $\overline{\sigma}$ denotes the standard deviation of the roughness.

B. Deduction of average Reynolds equation (macroscale)

For isoviscous, steady-state, and incompressibility fluid, the averaged Reynolds equation at the macroscopic scale can be expressed as

$$\frac{\partial}{\partial x}\left(\phi_{px}\frac{h^3}{12\mu}\frac{\partial p}{\partial x}\right)+\frac{\partial}{\partial y}\left(\phi_{py}\frac{h^3}{12\mu}\frac{\partial p}{\partial y}\right)=\frac{U_x}{2}\frac{\partial h}{\partial x}+\frac{U_y}{2}\frac{\partial h}{\partial y}+\frac{U_x}{2}\sigma\frac{\partial\phi_{sx}}{\partial x}+\frac{U_y}{2}\sigma\frac{\partial\phi_{sy}}{\partial y}, \tag{13}$$

where ϕ_{px}, ϕ_{py}, ϕ_{sx}, and ϕ_{sy} are pressure flow factors and shear flow factors along x and y directions, respectively; U_x and U_y is the velocity of textured bearing along x and y directions, respectively.

The cavitation is expressed using the Fischer Burmeister function[27]

$$P+T-\mathrm{sqrt}(P^2+T^2)=0. \tag{14}$$

To numerically solve the Reynolds equation with cavitation effects using FEM, it is necessary to use an augmented Reynolds equation as follows:

$$\frac{\partial}{\partial x}\left(\phi_{px}\frac{h^3}{12\mu}\frac{\partial p}{\partial x}\right)+\frac{\partial}{\partial y}\left(\phi_{py}\frac{h^3}{12\mu}\frac{\partial p}{\partial y}\right)=\frac{U_x}{2}\frac{\partial h}{\partial x}\left(1-\left(T-\frac{h}{2}\frac{\partial T}{\partial x}\right)\right)+\frac{U_y}{2}\frac{\partial h}{\partial y}+\frac{U_x}{2}\sigma\frac{\partial\phi_{sx}}{\partial x}+\frac{U_y}{2}\sigma\frac{\partial\phi_{sy}}{\partial y}. \tag{15}$$

To solve this equation, an additional equation is required to address the cavitation model involving two unknown variables, T and P. The equation is given as follows:

$$FB=-\mathrm{test}(T)\times(P+T+\mathrm{eps}-\mathrm{sqrt}(P^2+T^2)), \tag{16}$$

where eps is a numerical parameter used to eliminate errors arising from the use of the square root function.

A gauge pressure of $p=0$ is applied at the inner and outer radius. The computational domain is the complete annular fluid domain, $r\in[r_{\min}, r_{\max}]$ and $\theta\in[0, 2\pi]$.

C. Coupling of micro- and macro-scales (AF-ARE method)

In this study, the average Reynolds equation based on average flow model (AF-ARE method) is employed to achieve cross-scale coupling between microscopic texture features and the macroscopic lubrication performance of the bearing. For each textured unit, four flow factors can be obtained, as discussed above. For the whole textured pad, for units in the smooth region, the film thickness is the actual thickness h_0, the pressure flow factors will be 1, and the shear flow factors will be 0; and the pressure is governed by the traditional Reynolds equation without flow factors. For units in the textured region, the film thickness is the nominal thickness h_{nom}, and the pressure is governed by the averaged Reynolds equation with the flow factors.

In this study, the nominal thickness is defines as $h_{nom}=h_0+h_d/2$, as shown in Fig. 11.

D. Discussion of time consumption based on average flow Reynolds models

To validate the accuracy of the average flow method, a textured thrust bearing is studied. The parameters are listed in Table I. The inner and outer diameters of the thrust pad are 120 and 210 mm, respectively. Water is used as the lubricant.

The positions and distributions of textures are illustrated in Fig. 12. The inner radius of the thrust pad is $r_1=60$ mm and outer radius is $r_2=105$ mm. Circular textures are uniformly distributed with equal angular spacing α in the circumferential direction and equal spacing l_r in the radial direction.

To evaluate the computational efficiency of the AF-ARE method in solving the lubrication characteristics of textured thrust bearings, numerical simulations are performed for textured thrust bearings with three different numbers of textures using both the classical Reynolds equation method (RE method) and the averaged Reynolds equation based on the average flow model (AF-ARE method). This study

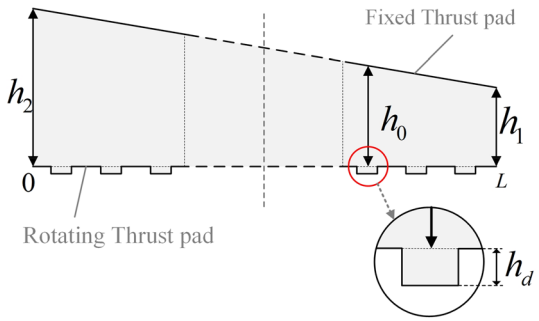

FIG. 11. Film thickness distribution in a texture unit. Textured regions use h_{nom} while smooth regions use the base thickness h_0.

TABLE I. Geometric parameters of bearing structure.

Parameters	Value
The inner diameter of the thrust pad (mm)	120
The outer diameter of the thrust pad (mm)	210
Dynamic viscosity (Pa·s)	0.00101

employs the Comsol partial differential equation (PDE) module for solving partial differential equations, coupled with MATLAB. For RE method, the textured thrust bearing is divided into a very fine mesh and numerically solving the classical Reynolds equation over the entire mesh. The parameters of the micro-textured thrust bearing are listed in Table II, including rotational speed, texture diameter D, texture depth h_d, film thickness at the maximum gap h_2, tilting ratio ratio$h$ (the ratio of minimum film thickness h_1 to maximum film thickness h_2), radial spacing l_r, circumferential spacing angle α, and texture number N. Under the same rotational speed, texture depth, maximum film thickness, and tilt ratio, only the texture diameter and quantity are varied to investigate the computational efficiency of the AF-ARE method.

The pressure distributions obtained from the two methods under three test cases are shown in Fig. 13, and the load capacities are listed in Table III. As shown in Fig. 13, the overall pressure distribution trends calculated by the RE method and the AF-ARE method are generally consistent. Due to the combined effects of tilt and texture, significant hydrodynamic pressure is generated. The pressure gradually increases when water flows into convergent region, with pressure peaks at the texture locations. It is noted that the dimensionless maximum pressure calculated by the RE method is higher than that obtained by the AF-ARE method, with differences of approximately 4.7%, 3.4%, and 1.5%, respectively. The main reason for this is that the RE method

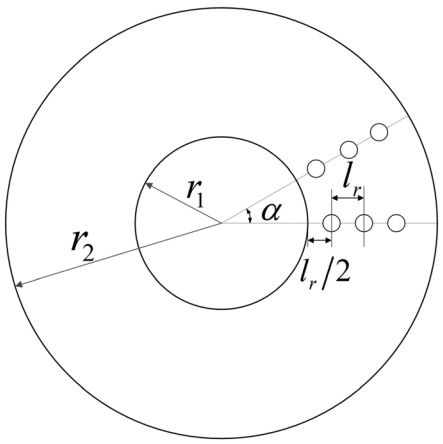

FIG. 12. Geometric parameters of textured thrust pad with circular dimples arranged uniformly in radial and circumferential directions.

retains more detailed microscale fluid flow features during numerical solving, such as local refined pressure gradient variations. In contrast, the AF-ARE method simplifies the lubrication behavior to some extent by introducing equivalent flow factors. Therefore, the AF-ARE method typically underestimates the pressure peaks in high-pressure regions.

The pressure distributions obtained from the two methods under three test cases are shown in Fig. 13, and the load capacities are listed in Table III. As shown in Fig. 13, the overall pressure distribution trends calculated by the RE method and the AF-ARE method are generally consistent. Due to the combined effects of tilt and texture, significant hydrodynamic pressure is generated. The pressure gradually increases when water flows into convergent region, with pressure peaks at the texture locations. It is noted that the dimensionless maximum pressure calculated by the RE method is higher than that obtained by the AF-ARE method, with differences of approximately 4.7%, 3.4%, and 1.5%, respectively. The main reason for this is that the RE method retains more detailed microscale fluid flow features during numerical solving, such as local refined pressure gradient variations. In contrast, the AF-ARE method simplifies the lubrication behavior to some extent by introducing equivalent flow factors. Therefore, the AF-ARE method typically underestimates the pressure peaks in high-pressure regions.

In summary, although there are certain differences in the maximum pressure, the AF-ARE method shows a high degree of consistency with the RE method in the overall pressure distribution trend, indicating that its computational results possess good accuracy and reliability.

The calculated load capacities by the RE method and AF-ARE method are listed in Table III. According to the results, the load capacities obtained by AF-ARE method demonstrate good agreement with

TABLE II. Parameters of textured micro-thrust bearing.

Case	Rotational speed (rpm)	D (μm)	h_d (μm)	h_2 (μm)	*ratioh*	l_r (mm)	α (deg)	N
1	5000	500	5	48	0.9	9	9	200
2	5000	400	5	48	0.9	6.43	9	280
3	5000	300	5	48	0.9	5	9	360

those by the RE method. The relative errors are only 0.06%, 0.10%, and 0.05%, respectively. These results indicate that the AF-ARE method maintains a high level of computational accuracy in solving the load capacity of textured bearings.

The time consumption and size of mesh needed using the two methods are presented in Table IV. It can be seen that, compared to the traditional RE method, the AF-ARE method significantly reduces the mesh size and computation time, thereby improving computational efficiency. As the texture diameter decreases and the mesh size increases, the reduction in time consuming exhausted by the AF-ARE method compared to the traditional RE method becomes more significant, with decreases of 36%, 42%, and 52%, respectively.

However, it should be noted that with the decrease in the diameter of micro-texture and increase in the texture quantity, the computation time exhausted by the AF-ARE method also increases significantly. This is because the AF-ARE method requires calculation of flow factors for each individual texture, and when the number of textures grows rapidly, the time needed to compute these flow factors increases substantially. Moreover, if there is need to optimize the micro-textured bearings, any structural changes require recalculation of the flow factors for each microscopic

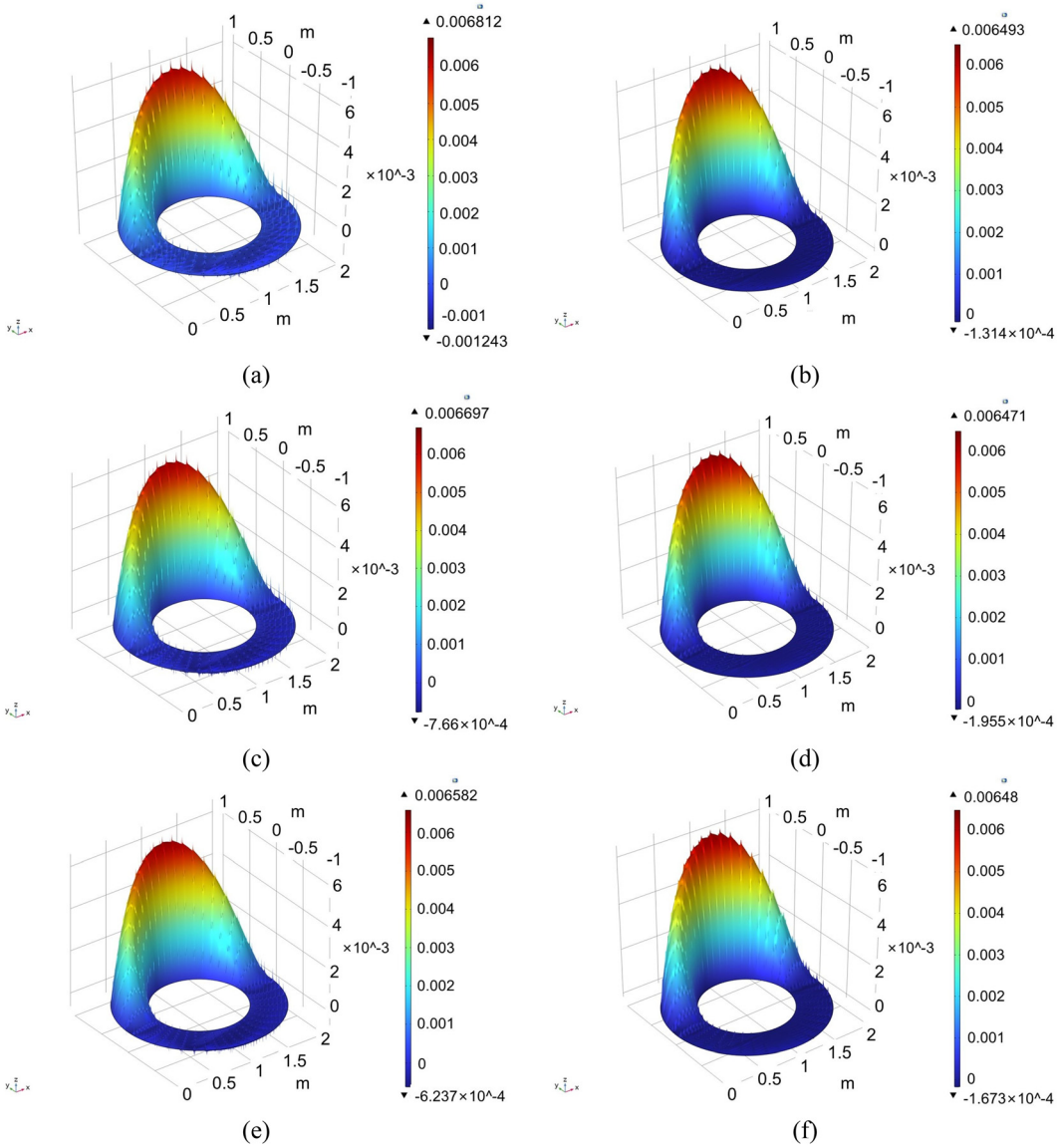

FIG. 13. Comparisons of pressure distribution between results by RE and AF-ARE methods. (a) Case 1 RE method, (b) case 1 AF-ARE method, (c) case 2 RE method, (d) case 2 AF-ARE method, (e) case 3 RE method, and (f) case 3 AF-ARE method. Both methods show similar overall patterns with minor local differences.

TABLE III. Comparisons of load capacity between results by RE and AF-ARE methods.

Case	Method	Load capacity (N)	Relative error (%)
1	RE	79.251	0.06
	AF-ARE	79.298	
2	RE	79.217	0.10
	AF-ARE	79.296	
3	RE	79.213	0.05
	AF-ARE	79.250	

texture, which significantly increasing the complexity of the optimization procedure.

III. DEVELOPMENT OF AN AVERAGED REYNOLDS EQUATION MODEL INTEGRATING THE AVERAGE FLOW MODEL AND MACHINE LEARNING ALGORITHM

To address the challenges of low computational efficiency of the AF-ARE method when dealing with bearing with high density microtextures and optimization design, this study proposes applying machine learning algorithms to predict the flow factors based on few calculations of flow factors to replace calculations of flow factors for each texture. First, an orthogonal experimental design is used to efficiently generate combinations of structural parameters for calculating flow factors, resulting in four small datasets. Then, these datasets are used to train machine learning models for predicting the respective flow factors. Finally, the predictive models are integrated with the average flow Reynolds model to perform numerical calculations.

A. Construction of flow factor datasets based on orthogonal experimental design

The orthogonal experimental design can efficiently replace full factorial experiments by covering all parameter combinations with a reduced number of trials.

To enable accurate prediction of flow factor values under various operating conditions and texture parameters, as shown in Fig. 14, the diameter of the circular texture (D), the velocity component in the x-direction (U_x), the velocity component in the y-direction (U_y), the depth of the circular texture (h_d), and the tilting ratio (*ratioh*) (since the diameter of the thrust pad and the maximum film thickness remain constant in this orthogonal experiment, the *ratioh* is defined as the ratio of the film thickness at the minimum gap to that at the maximum gap of the inclined thrust pad) are adopted as the main factors in the orthogonal design table. To ensure the applicability of the research results, the parameter ranges were determined based on the literature review, typical values from practical engineering applications, and manufacturing precision. Specifically, the diameter of the circular texture was set within the range of 200–800 μm and the depth within 2–20 μm. The velocity components in the x and y directions were selected to cover a wide range of rotational speed conditions. In actual manufacturing, due to manufacturing precision requirements, the tilting ratio of the thrust pad typically remains close to 1, even under misaligned loading. So the tilting ratio for a single texture unit was set within the range of 0.98–1. Based on the defined parameter ranges and levels, a five-factor, nine-level orthogonal design $L_{81}(9^5)$ was adopted. Part of the specific levels for each factor is listed in Table V.

Flow factors for each texture unit were derived according to the parameter combinations defined previously, following the flow factor calculation procedure. The obtained values were then normalized using the min-max method, expressed mathematically as

$$x' = (x - x_{\min})/(x_{\max} - x_{\min}). \tag{17}$$

In this expression, x' refers to the normalized form of an input flow factor, x is the original parameter value, and $x_{\min}$ and $x_{\max}$ indicate the smallest and largest values among the inputs, respectively.

These 81 sets of data constitute four separate datasets, each corresponding to one flow factor. Part of the results is listed in Table VI.

B. Flow factor prediction model based on machine learning algorithms

Based on the multiple sets of flow factor datasets obtained from the aforementioned research, a random partitioning strategy was employed to divide the data into a training set (70%), a validation set (15%), and a test set (15%), with the random seed set to 42. All data partitioning processes strictly adhered to the principle of randomness. Given the limited size of the available training samples, to avoid potential overfitting issues during modeling, this study selected three machine learning algorithms suitable for small-sample scenarios: support vector machines (SVM), extreme learning machines (ELM), and Gaussian process regression (GPR). The specific research process is as follows: first, for the training set of the four flow factors, the three machine learning prediction models mentioned above are constructed separately. Then, the validation set is used to evaluate performance and select the optimal model. Finally, the test set is used to verify the generalization performance of the selected model.

TABLE IV. Comparisons of time consuming between results by RE and AF-ARE methods.

Case	Method	D (μm)	N	Mesh size	Time consuming (h)	Difference of time (h)
1	RE	500	200	643870	12.5	4.5
	AF-ARE	500	200	18000	8	
2	RE	400	280	776330	16.5	7
	AF-ARE	400	280	20160	9.5	
3	RE	300	360	855908	22	11.5
	AF-ARE	300	360	25920	10.5	

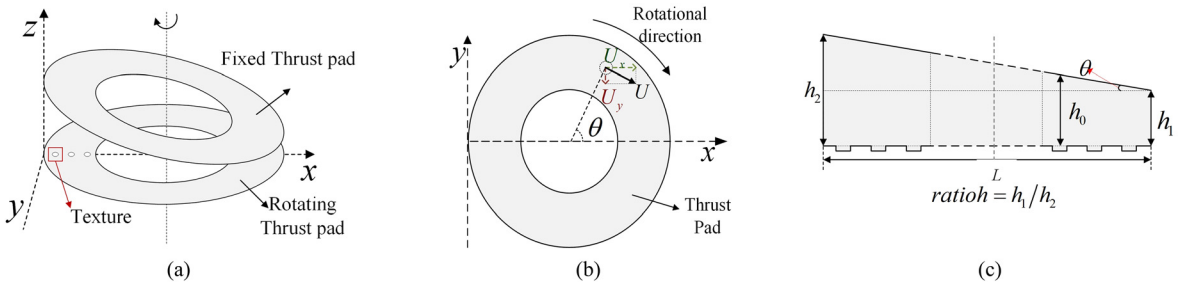

FIG. 14. Schematic of thrust bearing. (a) Three-dimensional structural diagram of thrust pad, (b) top view of thrust pad, and (c) front view of thrust pad.

1. Machine learning algorithms

SVM is a supervised learning algorithm based on statistical learning theory. The core idea of SVM is to construct an optimal regression function to minimize the deviation between the predicted values and the actual values. Specifically, SVM regression aims to find a function such that most sample points lie within an ε-band centered on the function, while allowing a few sample points to fall outside this range. This mechanism enhances the model's robustness and reduces the risk of overfitting to outliers. SVM regression achieves model training by optimizing the following loss function: where ε_i represents the prediction error of the ith sample point and C is the regularization parameter that balances the model's fitting error and structural complexity. ε is the tolerance threshold, allowing the model to remain robust against prediction errors with absolute values smaller than ε.

The extreme learning machine (ELM) is an efficient learning algorithm based on a single-layer feedforward neural network architecture. Its core idea is to randomly initialize the connection weights and biases from the input layer to the hidden layer and then directly solve the output layer weight matrix through analytical methods, thereby avoiding the iterative optimization process based on gradient descent in traditional neural networks. In ELM, for a given input vector x, the network output can be expressed as

$$F = H\beta, \tag{18}$$

where F represents the network's predicted output matrix, H represents the hidden layer output matrix, $H_{ij} = g(w_j \cdot x_i + b_j)$, where $g(x)$ is the activation function, w_j and b_j are the random weights and biases of the jth hidden layer neuron, and x_i is the input vector of the ith sample. β is the output weight matrix, where $\beta = H^{\dagger}T$ and T is the target

TABLE V. L81(9^5) orthogonal test table.

Case	D (μm)	U_x (m/s)	U_y (m/s)	h_d (μm)	*ratioh*
1	725	−110	83	2	0.9875
2	575	83	124	6.5	0.9875
3	425	165	−55	11	0.995
4	575	42	42	13.25	0.9925
5	800	−1	−165	17.75	0.9925
6	425	83	42	20	0.985
7	200	42	165	4.25	0.9875
8	575	165	1	17.75	0.9825
9	425	124	165	2	0.99
10	275	1	−165	8.75	0.995
⋮	⋮	⋮	⋮	⋮	⋮
72	500	1	1	11	0.99
73	500	83	−165	13.25	0.9975
74	200	−55	83	20	0.9975
75	800	42	83	8.75	0.98
76	425	1	83	17.75	1
77	200	124	1	6.5	0.995
78	275	−55	1	13.25	0.9875
79	575	−55	−1	2	0.995
80	650	1	−110	20	0.9875
81	725	42	−55	15.5	0.99

TABLE VI. Orthogonal test data for flow factors after normalization.

Case	Φ_{px}	Φ_{py}	Φ_{sx}	Φ_{sy}
1	0.999 224 25	0.999 505 034	0.167 552 513	0.184 367 601
2	0.763 831 192	0.763 979 096	0.440 788 797	0.454 089 061
3	0.503 485 984	0.503 272 148	0.445 143 277	0.444 013 109
4	0.370 844 959	0.370 609 476	0.661 200 043	0.668 218 875
5	0.121 046 857	0.120 659 901	0.985 157 298	1
6	0.002 506 087	0.002 279 735	0.483 220 579	0.493 398 315
7	0.886 765 339	0.886 981 11	0.067 583 233	0.063 685 608
8	0.116 020 264	0.115 981 786	0.673 118 815	0.695 203 837
9	0.999 413 546	0.999 593 821	0.077 480 291	0.079 043 96
10	0.635 918 991	0.635 778 828	0.234 820 583	0.229 374 73
⋮	⋮	⋮	⋮	⋮
72	0.501 746 226	0.501 660 114	0.526 294 409	0.533 831 334
73	0.372 831 631	0.372 533 078	0.575 156 861	0.573 096 306
74	0.008 920 743	0.008 418 411	0.205 106 458	0.196 854 01
75	0.631 571 352	0.632 035 55	0.757 333 006	0.798 163 43
76	0.124 613 954	0.124 163 308	0.506 575 223	0.500 448 012
77	0.765 384 888	0.765 310 233	0.120 101 922	0.112 398 3
78	0.368 823 482	0.368 738 628	0.281 837 483	0.282 288 547
79	0.999 744 726	0.999 792 047	0.133 644 554	0.131 767 4
80	0.003 984 013	0.003 673 7	0.774 993 142	0.792 969 588
81	0.241 840 613	0.241 595 913	0.871 879 415	0.888 867 919

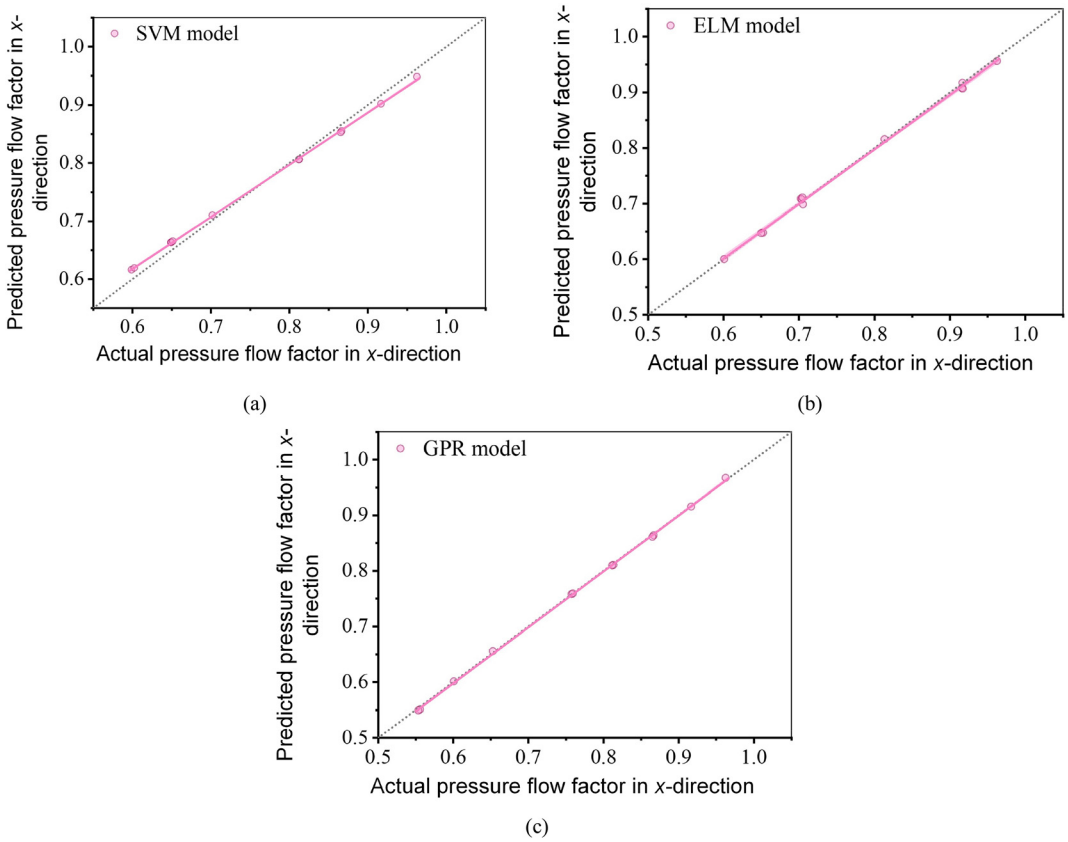

FIG. 15. Comparison of actual values and predicted values of pressure flow factors in the *x*-direction for different ML models. (a) Comparison of SVM model prediction values and actual values for pressure flow factors in the *x*-direction, (b) comparison of ELM model prediction values and actual values for pressure flow factors in the *x*-direction, and (c) comparison of GPR model prediction values and actual values for pressure flow factors in the *x*-direction. The GPR model achieves the best agreement.

output matrix. $H^{\dagger}$ is the output layer weights obtained by computing the Moore–Penrose generalized inverse matrix of H. This allows ELM to ensure that the model has a certain degree of generalization while also having a fast training speed.

Gaussian process regression (GPR) is a nonparametric probabilistic model based on the Bayesian framework, suitable for tasks, such as small sample learning, high-dimensional data modeling, and uncertainty quantification. Unlike traditional parametric regression methods, it does not make explicit assumptions about the form of the function but instead directly defines a probability distribution in the function space, thereby making it possible to model complex data relationships. In GPR, the hypothesis function $f(x)$ is assumed to follow a Gaussian process

$$f(x) \sim \mathcal{GP}(m(x), k(x, x')), \tag{19}$$

where $m(x)$ represents the mean function, while $k(x, x')$ represents kernel function.

The hyperparameters of SVM, ELM, and GPR were all selected via grid search to achieve optimal performance of the machine learning models. During the training of the machine learning models, GPU acceleration was not utilized. All models were run on an Intel i5 processor with 32 GB of memory under the Windows 10 64-bit operating system, using MATLAB as the programing environment.

2. Evaluation metrics for predictive models

In this study, the mean absolute error (MAE), mean squared error (MSE), and coefficient of determination (R^2) were used to evaluate the constructed machine learning prediction models. The formulas are as follows:

$$\mathrm{MAE} = \frac{1}{n}\sum_{i=1}^{n} |y_i - \hat{y}_i|, \tag{20}$$

$$\mathrm{MSE} = \frac{1}{n}\sum_{i=1}^{n} (y_i - \hat{y}_i)^2, \tag{21}$$

$$\mathrm{R}^2 = 1 - \frac{\sum_{i=1}^{n} (y_i - \hat{y}_i)^2}{\sum_{i=1}^{n} (y_i - \bar{y})^2}, \tag{22}$$

where y_i represents the calculated value of the ith sample, $\hat{y}_i$ represents the predicted value of the ith sample, $\bar{y}$ is the mean of the calculated values, and n is the total number of samples. When the values of MAE and MSE are close to 0, and the R^2 value is close to 1, it indicates better

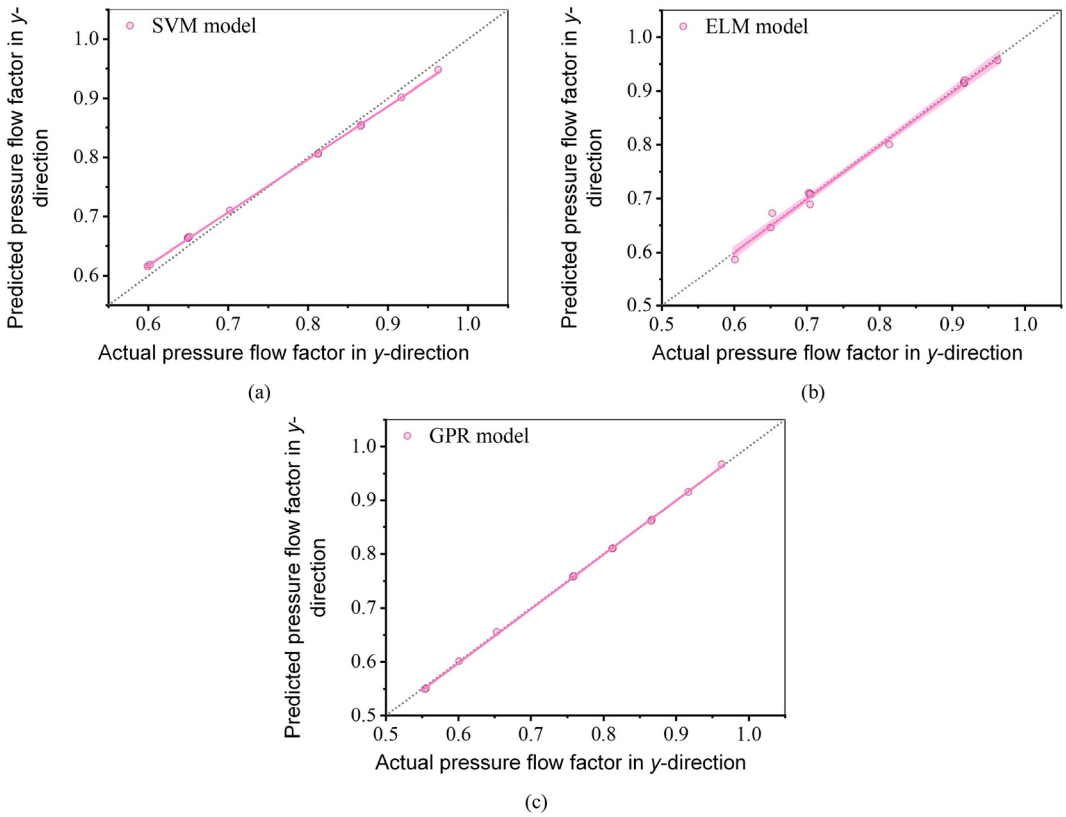

FIG. 16. Comparison of actual values and predicted values of pressure flow factors in the *y*-direction for different ML models. (a) Comparison of SVM model prediction values and actual values for pressure flow factors in the *y*-direction, (b) comparison of ELM model prediction values and actual values for pressure flow factors in the *y*-direction, and (c) comparison of GPR model prediction values and actual values for pressure flow factors in the *y*-direction. GPR shows the highest accuracy.

predictive performance of the model, with lower error between the predicted and actual values, it indicates that the model has a high degree of fit to the data.

C. Performance comparison of ML models

The performance comparison results of machine learning prediction models on the validation set are shown in Figs. 15–18. As shown in Figs. 15 and 16, in the prediction of pressure-flow factors, the GPR models exhibited the narrowest confidence interval and the linear fitting curve closest to the diagonal line, demonstrating superior prediction accuracy compared to the SVM and ELM models. In the prediction of shear-flow factors, as shown in Figs. 17 and 18, the predicted values from the GPR models' predicted values are closer to the calculated values, with a significantly narrower confidence interval width than the comparison algorithms, and the linear fit curve is also closer to the diagonal line. Comparing Fig. 15(a) with Fig. 17(a) and Fig. 15(b) with Fig. 17(b), it can be observed that the SVM and ELM models perform significantly poorer in shear-flow factor prediction than in pressure-flow factor prediction, indicating that these models have limitations in their overall predictive performance. In contrast, the GPR models demonstrate excellent and stable performance in predicting flow factors for both pressure flow and shear flow in all directions, validating its strong generalization capability.

Based on the evaluation metric formulas, the prediction performance of the three ML algorithms on the four flow factors was calculated using the validation dataset. The evaluation results of the three models are summarized in Table VII. According to the evaluation outcomes, the GPR models consistently demonstrated the best predictive performance across all four flow factors. The MAE values for the GPR models were 0.0063, 0.0063, 0.0113, and 0.0113; the corresponding MSE values were 5.68×10^{-5}, 5.71×10^{-5}, 2.107×10^{-4}, and 2.115×10^{-4}; and the R^2 values were 0.9995, 0.9995, 0.9975, and 0.9976, respectively. Clearly, the GPR models outperformed the SVM and ELM models, achieving significantly better consistency between predicted and actual values.

D. Generalization performance of GPR prediction mode

As discussed above, the GPR models are selected for the next step. In order to test the generalization performance of GPR prediction models, a test dataset, which has not been used before, is introduced. The comparisons between predicted results and true values for the four flow factors are shown in Fig. 19, and the evaluation criterias are listed in Table VIII.

The results indicate that the GPR prediction model constructed based on the four flow factors demonstrates excellent predictive

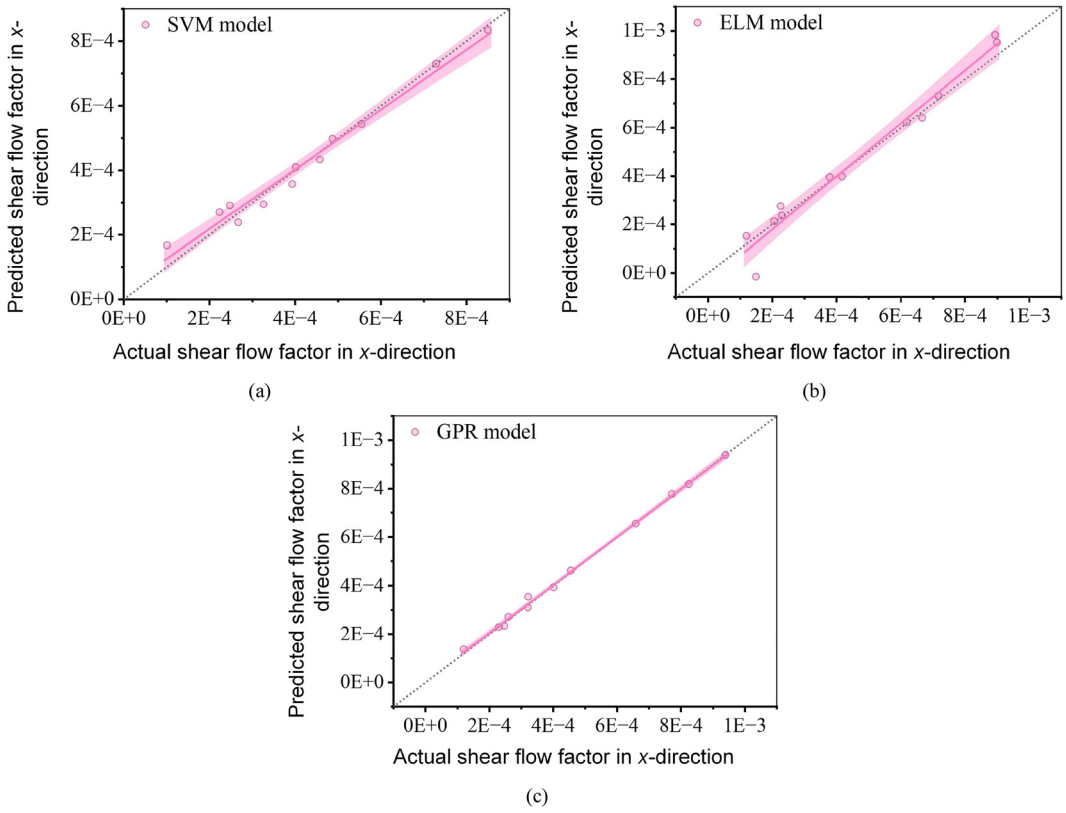

FIG. 17. Comparison of actual values and predicted values of shear flow factors in the *x*-direction for different ML models. (a) Comparison of SVM model prediction values and actual values for shear flow factors in the *x*-direction, (b) comparison of ELM model prediction values and actual values for shear flow factors in the *x*-direction, and (c) comparison of GPR model prediction values and actual values for shear flow factors in the *x*-direction. GPR predictions closely follow calculated values.

performance on the test set. As shown in Fig. 19, the predicted values of all flow factors are highly consistent with the actual values, with the data points closely distributed around the diagonal line. On the test set, the evaluation metrics (MAE and MSE) of the GPR models are close to 0, while the coefficient of determination R^2 is close to 1 ($R^2 > 0.99$). This indicates that (1) the established GPR prediction models can accurately find the relationship of flow factor data; (2) the model does not exhibit overfitting due to training data; and (3) the model demonstrates good generalization ability in predicting pressure and shear flow factors in all directions. Additionally, the models' prediction accuracy for shear flow factors ($R^2 = 0.997$) is comparable to that for pressure flow factors ($R^2 = 0.999$), further validating the stability of its predictive performance.

IV. COMPARISONS OF RESULTS BETWEEN AFML-ARE AND RE METHODS

To evaluate the accuracy and computational efficiency of the proposed AFML-ARE model, comparisons are made between the AFML-ARE and RE methods in terms of pressure distribution, load capacity, and computation time. Furthermore, to investigate the advantages of AFML-ARE in improving computational efficiency and its applicability under different conditions, the computation time required by the AFML-ARE method is evaluated under identical operating conditions as the number of textures increases and the texture diameter decreases (as shown in Table II). The results are compared with those obtained using the RE method and the AF-ARE method mentioned above.

A. Accuracy analysis of the AFML-ARE method

Numerical simulations are conducted for thrust pads under four operating conditions: 1500, 5000, 6000, and 7000 rpm. The calculation parameters for the micro-textures are listed in Table IX. The RE method and the AFML-ARE method are used to compute the pressure distribution and load capacity of the textured thrust bearing. The simulations are carried out using MATLAB in combination with the partial differential equation (PDE) module of COMSOL.

The pressure distributions obtained using the RE and AFML-ARE methods are shown in Fig. 20. The results indicate that the resulting pressure distributions obtained by the two methods are in excellent agreement. In the convergent wedge region (where film thickness decreases), hydrodynamic effects are generated, with pressure gradually accumulating along the flow direction and forming a significant peak within the textured region. This is followed by a rapid pressure drop in the divergent section (where film thickness increases). The relative errors in the dimensionless maximum pressure values obtained by the two methods are 1.59%, 3.23%, 3.97%, and 5.35% for the four cases with different parameters under various working conditions, respectively. The maximum error of peak pressure between the two methods

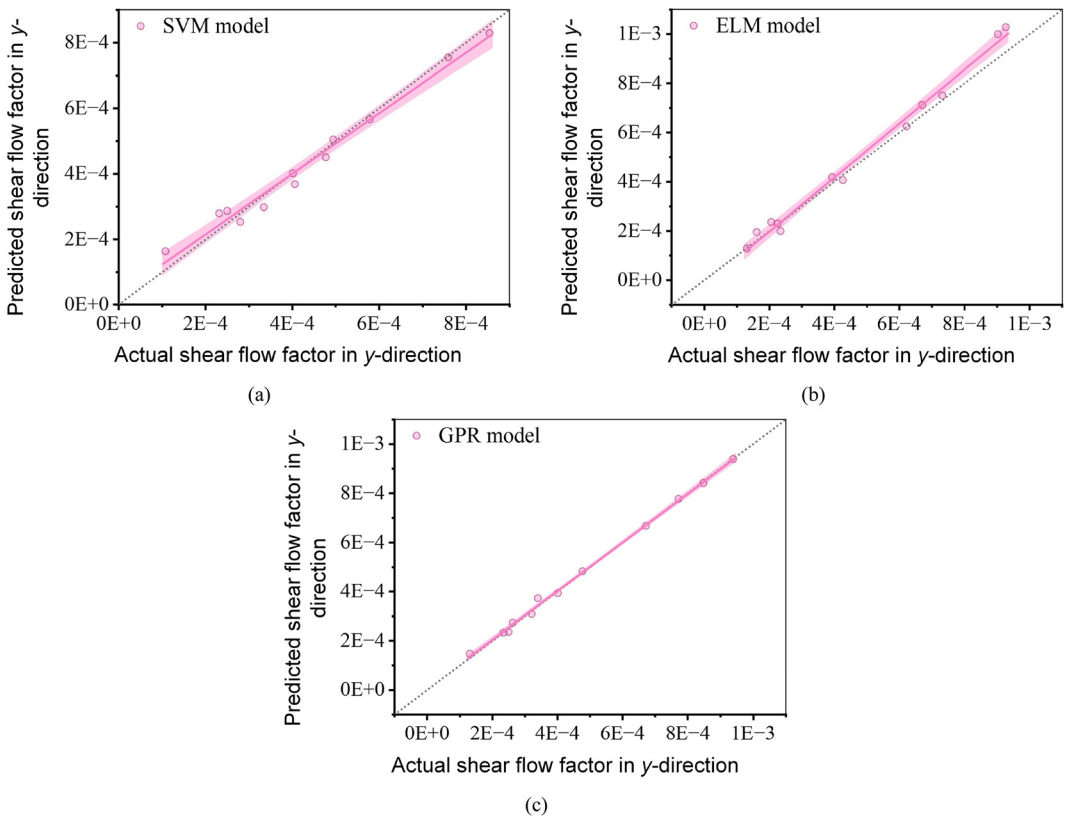

FIG. 18. Comparison of actual values and predicted values of shear flow factors in the *y*-direction for different ML models. (a) Comparison of SVM model prediction values and actual values for shear flow factors in the *y*-direction, (b) comparison of ELM model prediction values and actual values for shear flow factors in the *y*-direction, and (c) comparison of GPR model prediction values and actual values for shear flow factors in the *y*-direction. Good agreement is observed, especially for GPR.

is approximately 5.35%, with an average error of only 3.54%. This demonstrates that the proposed AFML-ARE method maintains good computational accuracy compared to the conventional RE method.

Table X presents a comparison of the bearing load capacity and computation time obtained using the two methods. As shown in the table, the load capacities calculated by the two methods are in excellent agreement. The maximum difference of the load capacity between the two methods is only 0.12%, further confirming the accuracy of the proposed AFML-ARE method.

TABLE VII. The evaluation results of the three ML models.

Flow factors	ML model	MAE	MSE	R^2
Φ_{px}	SVM	0.0303	1×10^{-3}	0.9891
	ELM	0.0120	2×10^{-4}	0.9978
	GPR	0.0063	5.68×10^{-5}	0.9995
Φ_{py}	SVM	0.0304	1×10^{-3}	0.9890
	ELM	0.0193	6×10^{-4}	0.9933
	GPR	0.0063	5.71×10^{-5}	0.9995
Φ_{sx}	SVM	0.0304	1.3×10^{-3}	0.9751
	ELM	0.0449	4.5×10^{-3}	0.9529
	GPR	0.0113	2.107×10^{-4}	0.9975
Φ_{sy}	SVM	0.0305	1.3×10^{-3}	0.9773
	ELM	0.0386	2.7×10^{-3}	0.9729
	GPR	0.0113	2.115×10^{-4}	0.9976

To further assess the impact of prediction errors in flow factors, a sensitivity analysis was performed by uniformly perturbing all flow factors by ±2%. The results show that the corresponding variation in bearing load capacity is limited to −1.97% and +2.05%. This indicates that moderate uncertainties in ML-predicted flow factors lead to only minor deviations in performance metrics, confirming that the AFML-ARE framework remains robust under such perturbations.

B. Computational efficiency of AFML-ARE method

To further evaluate the computational efficiency advantage of the proposed AFML-ARE method, three textured bearings listed in Table II are also analyzed using the AFML-ARE method. The pressure distributions obtained by AFML-ARE are shown in Fig. 21. The computation time for each method is also summarized in Table XI. The results show that, for the three cases, the AFML-ARE method reduces computation time by 48%, 55%, and 64% compared to the RE method, and by 19%, 21%, and 24% compared to the AF-ARE method, respectively. This improvement in computational efficiency is primarily attributed to the integration of a machine learning-based flow factor prediction

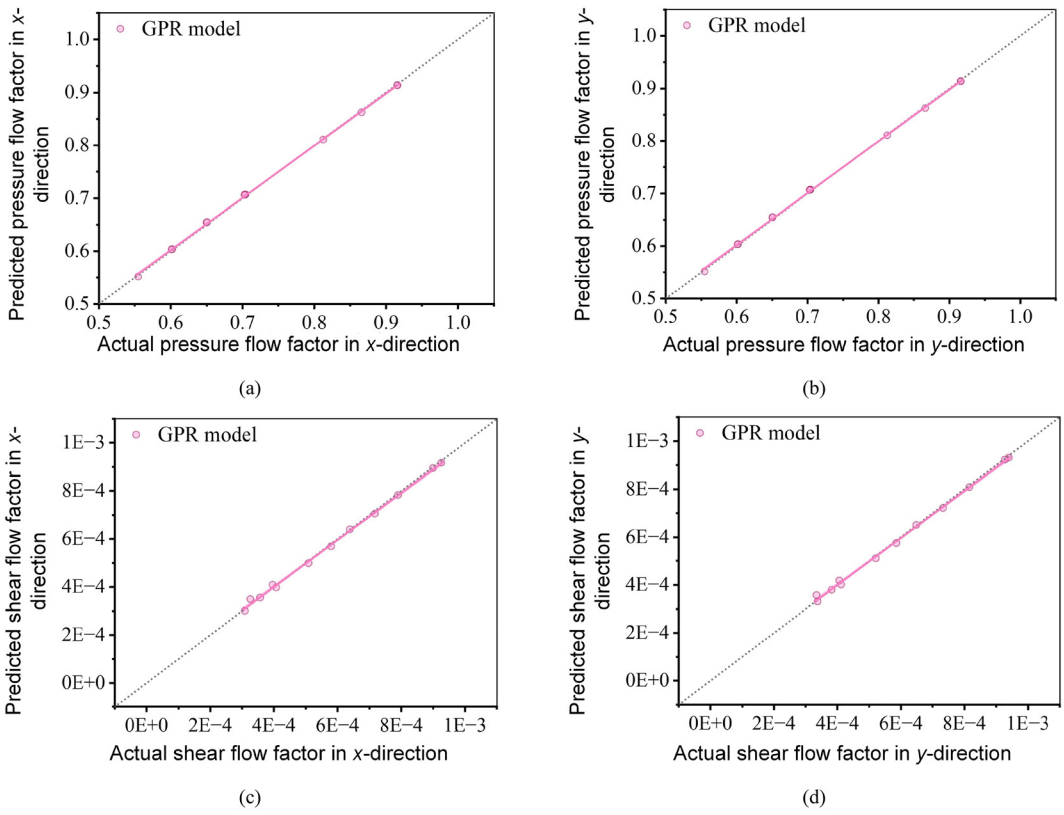

FIG. 19. Comparison of GPR model prediction values and actual values for flow factors. (a) Comparison of prediction values and actual values for pressure flow factors in the *x*-direction, (b) Comparison of prediction values and actual values for pressure flow factors in the *y*-direction, (c) Comparison of prediction values and actual values for shear flow factors in the *x*-direction, and (d) Comparison of prediction values and actual values for shear flow factors in the *y*-direction. Predictions align closely with test data.

model within the AFML-ARE method. These data-driven model effectively eliminates the need for individually computing each flow factor for all the textures as required in the AF-ARE method, while also avoiding the numerical inefficiency caused by mesh refinement in the traditional RE method when analyzing high-density micro-textured bearings.

It is worth noting that as the texture density increases and the texture diameter decreases (from 500 to 300 μm), the computation time for both methods increases. However, the rate of increase differs significantly between the two methods. For case 1 with 200 textures of diameter 500 μm, the computation time difference for the two methods is 6 h; however, when it comes to case 3, the computation time for the AFML-ARE method is about 8 h, while that for the RE method reaches 22 h, leading to a difference of 14 h. It is noted that, in case 1, AFML-ARE reduces computation time by 48% relative to RE and 18.8% relative to AF-ARE. In case 2, the reductions are 54.5% and 21.1%, respectively. In case 3, the computation time is reduced by 63.6% compared with RE and by 23.8% compared with AF-ARE. These results demonstrate that the AFML-ARE method has better computational efficiency for solving high-density micro-textured bearings.

TABLE VIII. Evaluation metrics for the accuracy of GPR model predictions of flow factors in the test set.

ML model	Flow factor	MAE	MSE	R^2
GPR	Φ_{px}	0.0068	0.0496×10^{-3}	0.9994
	Φ_{py}	0.0068	0.0501×10^{-3}	0.9994
	Φ_{sx}	0.0108	0.1511×10^{-3}	0.9974
	Φ_{sy}	0.0109	0.1534×10^{-3}	0.9974

V. INTELLIGENT OPTIMIZATION DESIGN OF MICRO-TEXTURED THRUST BEARINGS USING PARTICLE SWARM OPTIMIZATION ALGORITHM

Based on the previously developed AFML-ARE model, this study incorporates an intelligent optimization algorithm, particle swarm

TABLE IX. Parameters of micro-textured bearing.

Case	Rotational speed (rpm)	D (μm)	h_d (μm)	h_2 (μm)	*ratioh*	N
1	1500	500	9	85	0.8	200
2	5000	600	3	22	0.8	240
3	6000	700	2	17	0.8	200
4	7000	800	2	14	0.8	240

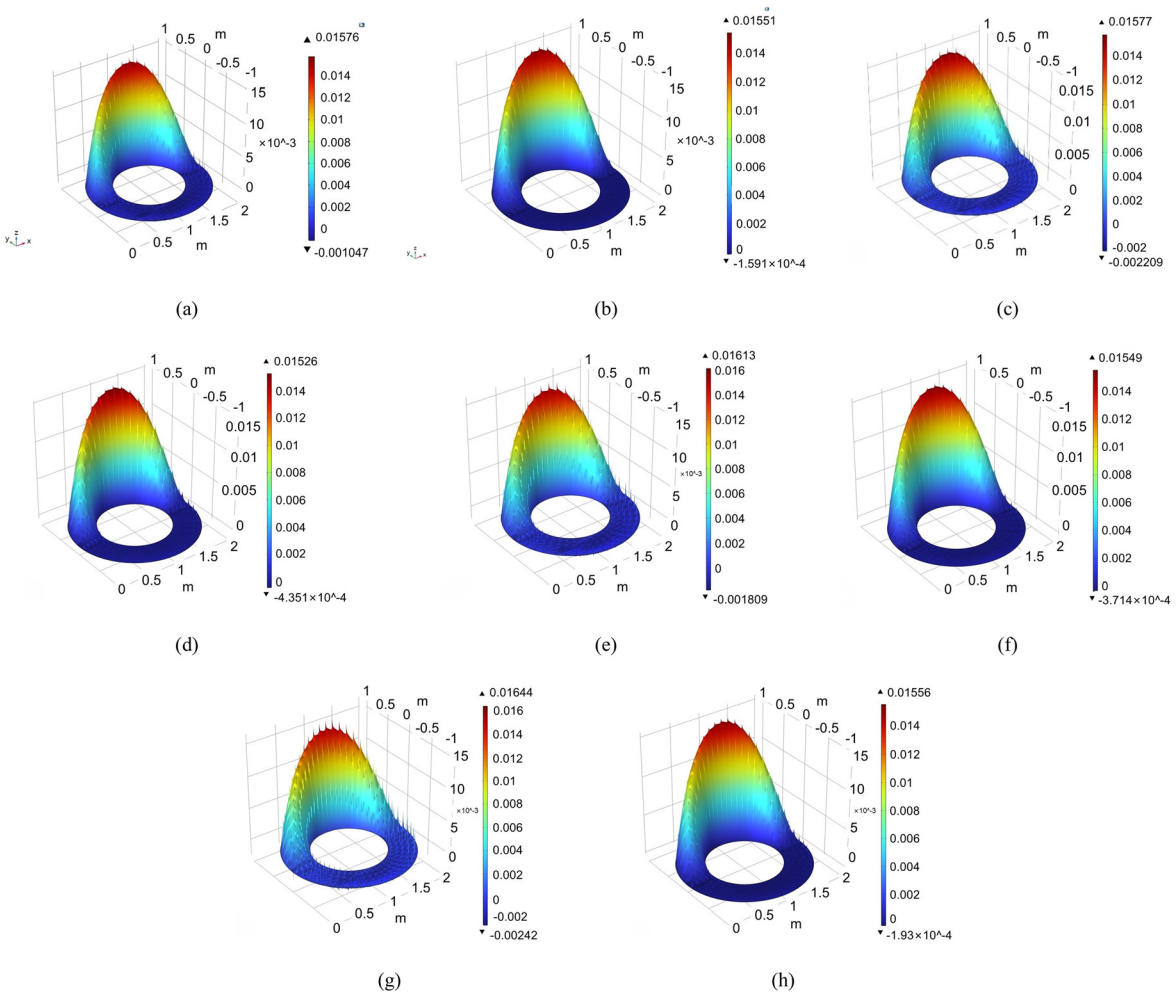

FIG. 20. Comparisons of pressure distribution between RE and AFML-ARE methods at different speeds. (a) RE 1500 rpm, (b) AFML-ARE 1500 rpm, (c) RE 5000 rpm, (d) AFML-ARE 5000 rpm, (e) RE 6000 rpm, (f) AFML-ARE 6000 rpm, (g) RE 7000 rpm, and (h) AFML-ARE 7000 rpm. The AFML-ARE results agree well with RE predictions.

optimization (PSO), to maximize the load capacity of textured thrust bearings. The design variables include the diameter of the circular texture, the depth ratio (defined as the ratio of texture depth to the maximum film thickness of the pad), the radial spacing of textures, and the circumferential spacing angle. By employing PSO, an intelligent optimization design of the micro-textured, water-lubricated thrust bearing is carried out.

Particle swarm optimization (PSO) is a population-based stochastic optimization technique inspired by the social behavior of birds flocking. PSO is widely used due to its simplicity, low computational cost, and effectiveness in solving nonlinear, multidimensional, and complex optimization problems. The basic flow chart of the PSO algorithm is illustrated in Fig. 22. In this model, the velocity update equation is given by

$$v_i(t+1) = \omega \cdot v_i(t) + c_1 \cdot r_1 \cdot \left(pbest_i - x_i(t)\right) + c_2 \cdot r_2 \cdot \left(gbest - x_i(t)\right), \tag{23}$$

where $v_i(t)$ denotes the velocity of particle i at iteration t, $x_i(t)$ represents the position of particle i at the same iteration, and ω is the inertia weight, which controls the influence of the particle's previous velocity on its current motion; c_1 and c_2 are cognitive and social learning

TABLE X. Comparisons of load capacity between RE and AFML-ARE methods.

Case	Method	Load capacity (N)	Relative difference ratio (%)
1	RE	18.05	0.11
	AFML-ARE	18.07	
2	RE	897.57	0.09
	AFML-ARE	898.36	
3	RE	1804.2	0.09
	AFML-ARE	1805.8	
4	RE	3104.4	0.12
	AFML-ARE	3108.1	

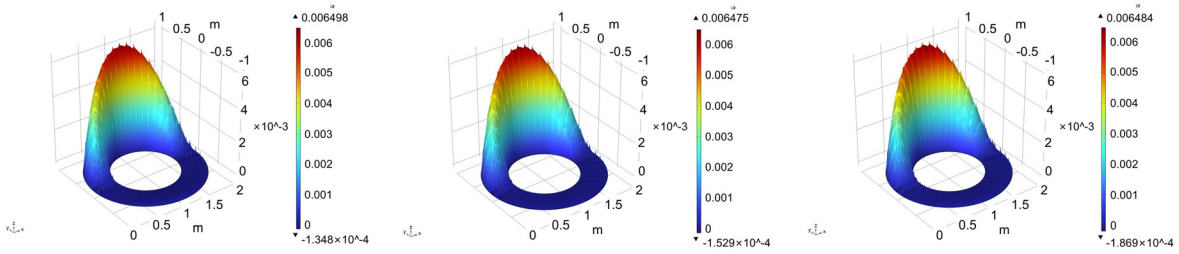

(a) (b) (c)

FIG. 21. Pressure distributions calculated by AFML-ARE for three texture cases. The method shows robustness across texture geometries. (a) case 1, (b) case 2, and (c) case 3.

factors, respectively, which regulate the particle's tendency to move toward its own best-known position and the global best position found by the swarm. r_1 and r_2 are random numbers uniformly distributed in the interval [0, 1], introducing stochastic variability to the particle's trajectory. $pbest_i$ denotes the personal best position found by particle i, while gbest refers to the global best position identified by the entire swarm.

The position update equation is given by

$$x_i(t+1) = x_i(t) + v_i(t+1), \tag{24}$$

where $x_i(t+1)$ is the updated position of particle i at iteration $t+1$, $x_i(t)$ is the current position, and $v_i(t+1)$ is the updated velocity of the particle.

Utilizing a micro-textured, water-lubricated thrust bearing with parallel plates as a case study, a dynamic intelligent optimization design procedure was carried out at a rotational speed of 1500 rpm. Constrained by the precision of fabrication, the diameter of the circular texture D, is assumed to fall within the range of 500–1000 μm; the depth ratio *ratioh* ranges from 0.1 to 0.3; the radial texture spacing lr is set between 3 and 9 mm; and the circumferential spacing angle α is varied from 6° to 12°.

Figure 23 presents the fitness convergence curve obtained from the optimization algorithm. According to the results, the algorithm demonstrates a rapid convergence trend within the first 10 generations, with the fitness value increasing by approximately 21%. By the 34th iteration, the fitness value becomes nearly stable, indicating that the proposed optimization model exhibits good convergence stability. The bearing load capacities before and after optimization are listed in Table XII. The optimized micro-texture parameters are rounded as follows: the texture diameter is rounded to 999 μm, the depth ratio remains at 0.3, the radial texture spacing l_r is rounded to 3.214 mm, and the circumferential spacing angle α is rounded to 9°. After optimization, the load capacity of the micro-textured water-lubricated bearing increases from 5.5 to 12.4 N, with a 126% improvement, demonstrating the effectiveness of the intelligent optimization approach in improving the performance of micro-textured water-lubricated thrust bearings.

TABLE XI. Comparion of computation time needed by three methods.

Case	Methods	D (μm)	N	Computing time (h)	Difference of computing time between other methods and AFMLARE (h)
1	RE	500	200	12.5	6
	AF-ARE	500	200	8	
	AFML-ARE	500	200	6.5	
2	RE	400	280	16.5	9
	AF-ARE	400	280	9.5	
	AFML-ARE	400	280	7.5	
3	RE	300	360	22	14
	AF-ARE	300	360	10.5	
	AFML-ARE	300	360	8	

VI. EXPERIMENTAL VALIDATION

A. Experimental apparatus

To validate the accuracy of the proposed AFML-RE method, an experimental apparatus was designed and manufactured to test the film thickness of a water-lubricated thrust disk. Micro-textures were fabricated on the surface of the thrust disk using femtosecond laser processing technology. Femtosecond laser micromachining is widely recognized for its high precision and reproducibility. Bhaduri *et al.*[28] reported that state-of-the-art laser micromachining platforms exhibit repeatability better than 2 μm and reproducibility better than 6 μm. Under a constant load, the water film thickness of the textured water-lubricated thrust bearing was measured at various rotational speeds.

As shown in Fig. 24, the experimental apparatus is composed of four main components: a motor, textured thrust pad, measurement system, and support frame. The motor system consists of a motor, a variable frequency drive (VFD), and a coupling. The power is transmitted to the rotating disk via the coupling, enabling the system to rotate at a predetermined speed.

The thrust bearing consists of an upper and a lower thrust disk, lubricated by water. During the experiment, the motor drives the shaft to rotate the lower stainless-steel disk. The surface of the upper disk is micro-textured, while the lower disk is filled with water. Both disks are needed to be polished to achieve a surface roughness of 0.02 μm.

The measurement system includes laser displacement sensor and a computer. The sensor is responsible for detecting variations in the water film thickness between the two thrust disks. Since the film thickness is typically on the order of tens of micrometers, high-precision displacement sensor is required. In this study, the LK-P25 laser displacement sensor from the P series, manufactured by Zhongguang

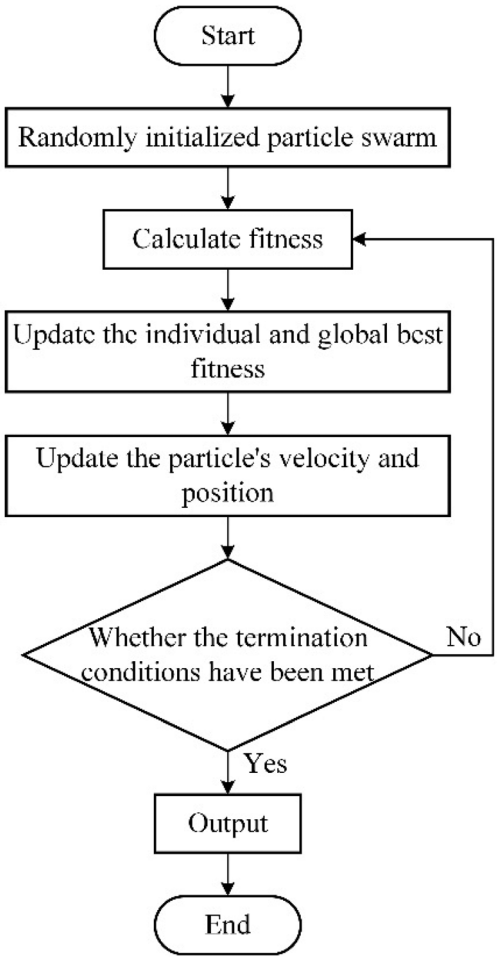

FIG. 22. Flowchart of the PSO algorithm. Texture parameters are optimized to maximize load capacity.

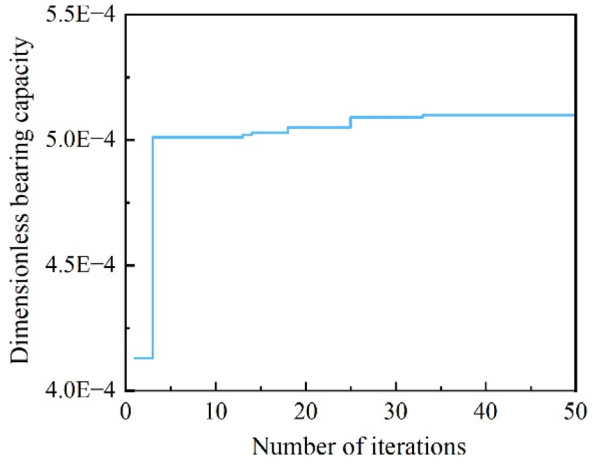

FIG. 23. Fitness convergence curve of PSO optimization.

TABLE XII. Comparison before and after optimization.

	D (μm)	*ratioh*	l_r (mm)	α (deg)	Load capacity (N)
Before optimization	800	0.3	4.5	9	5.4827
After optimization	999.4	0.2998	3.0058	9.1956	12.401

Automation Technology Co., Ltd., is used to ensure measurement accuracy.

All experiments were conducted at room temperature using pure de-ionized water, which was replaced before each run to ensure consistency and to avoid contamination that might affect film thickness and load capacity. The tests were carried out in a laboratory environment with ambient temperature maintained at approximately 25 °C. A calibrated thermometer was used to record the water temperature before and after each run, and the variation was found to be within 2 °C. Considering the relatively low rotational speeds used in this study and the low viscosity of water, the resulting temperature rise was negligible and had no significant effect on the lubrication performance.

B. Fabrication of the textured thrust disk

In this study, a mirror-polished 304 stainless steel was selected as the base material for the textured thrust disk, with a surface roughness of 0.02 μm. Micro-textures were fabricated using a femtosecond laser system (model: LR-femto1030-30). The key processing parameters for laser texturing are listed in Table XIII. During fabrication, the number of laser scan passes was adjusted to approximately five to achieve the desired texture depth. The laser processing was conducted at a repetition rate of 50 kHz, a scanning speed of 100 mm/s, and a pulse energy of 10 μJ. The fabricated textured thrust disk samples are shown in Fig. 25.

C. Measurement of water film thickness

Limited by the actual manufacturing precision and vibration, the film thickness is tested under the rotary speed of 400, 600, 800, 1000, 1500, and 2000 rpm. To simplify the loading system and ensure a stable load, the self-weight of the upper thrust disk (5 N) was used as a constant vertical load during the tests. The thrust disk was made of 304 stainless steel, with structural parameters listed in Table XII. The inner diameter is 120 mm and outer diameter is 210 mm.

To assess the repeatability of the film thickness measurements, two repeated measurements were conducted at each rotational speed. The deviations between repeated tests were generally within 3%, indicating good repeatability. The water film thickness was measured using an LK-P25 displacement sensor, which provides a resolution of 0.01 μm.

1. Experimental results of the textured thrust bearing before optimization

As listed in Table XII, before optimization, the micro-textured thrust disk had a texture diameter of 800 μm, a depth of 15 μm, 10 textures along the radial direction, and 40 textures along the circumferential direction, resulting in a total of 400 textures. To reduce

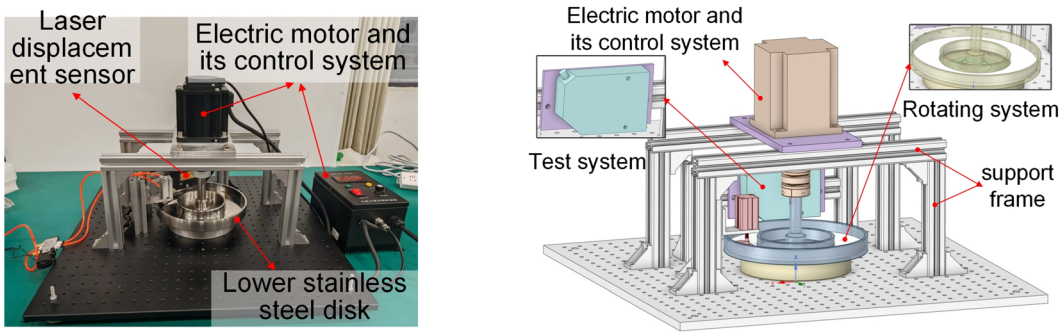

FIG. 24. Experimental apparatus for film thickness measurement. (a) Photograph of the rig and (b) 3D model.

TABLE XIII. Parameters for laser texturing.

Items	Value
Maximum output power (W)	30
Central wavelength (nm)	1030
Frequency (kHz)	50
Spot diameter (μm)	30
Pulse width (fs)	400

measurement noise, the measured data were processed using a smoothing function. The experimental results of water film thickness under different rotational speeds with the same self-weight of the upper thrust disk are shown in Fig. 26.

Under the self-weight of the upper thrust disk, the measured film thickness exhibited significant fluctuations due to incomplete formation of the hydrodynamic effect, leading to possible localized micro-contact. Therefore, the first 20 s of data are excluded from the analysis. As shown in the figures, the water film gradually developed and eventually exhibited a relatively stable trend with time.

The data from the final 20 s, during which the film thickness exhibited a relatively stable trend, were extracted, and their average value was calculated as the tested water film thickness under the given load and rotational speed. Meanwhile, the theoretical film thickness under the same conditions was calculated using the proposed AFML-RE method through iterative computation. A comparison between the experimental and theoretical results is shown in Fig. 27. The solid lines represent the theoretical values and the dashed lines represent the measurements.

The results indicate that, under constant load, the film thickness increases with the increasing rotational speed. At 400 rpm, the deviation between the experimental and theoretical values is only 9.4%. However, as the speed increases, the deviation gradually becomes larger, reaching a maximum of 11.8% at 2000 rpm. The average deviation is about 10.5%.

Considering vibration at high speeds, manufacturing errors, and measurement errors, the theoretical predictions are in good agreement with the experimental results. This confirms the accuracy and reliability of the proposed AFML-RE method.

2. Experimental results of the textured thrust bearing after optimization

As listed in Table XII, after optimization, the micro-textured thrust disk had a texture diameter of 999 μm, a depth of 8 μm, 14 textures along the radial direction, and 40 textures along the circumferential direction, resulting in a total of 560 textures. Figure 28 shows the

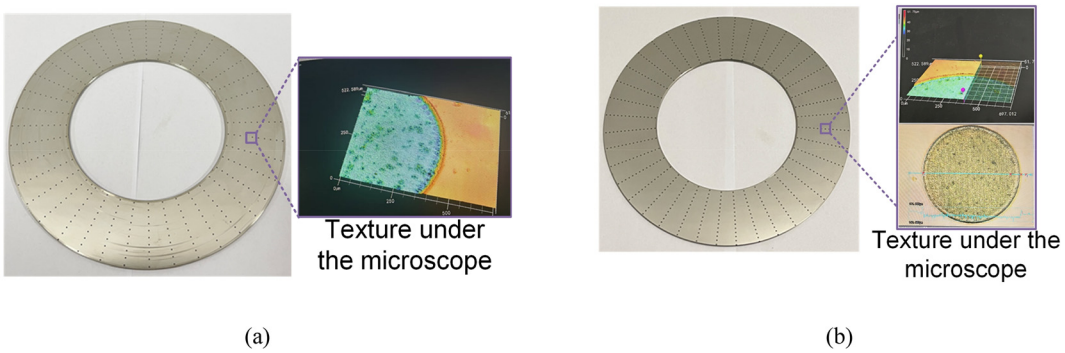

FIG. 25. Fabricated textured thrust pads: (a) textured thrust pad before optimization and (b) textured thrust pad after optimization using laser processing.

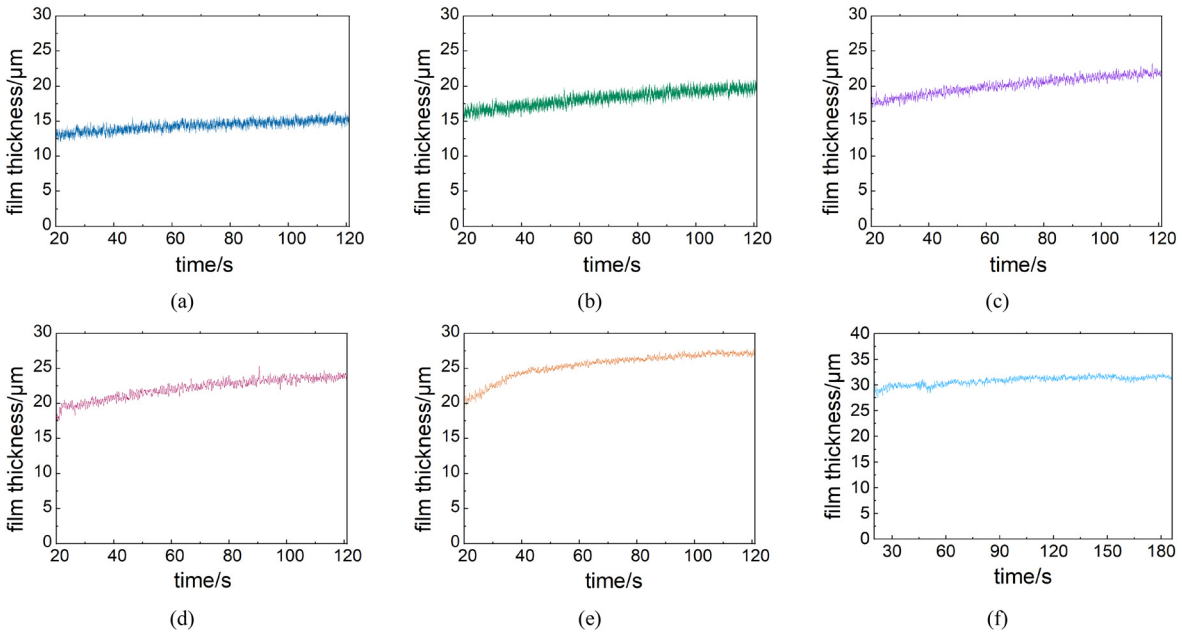

FIG. 26. Tested film thickness with different rotary speed. before optimization.(a) 400 rpm, (b) 600 rpm, (c) 800 rpm, (d) 1000 rpm, (e) 1500 rpm, and (f) 2000 rpm. Thickness increases with speed.

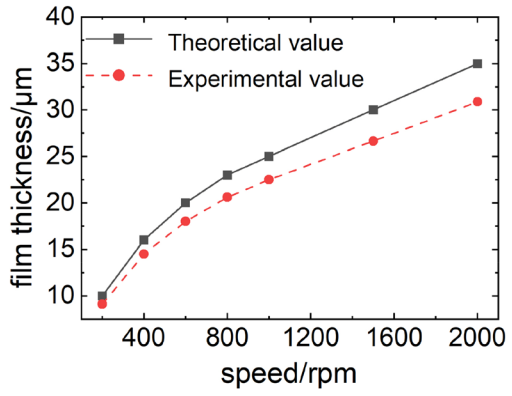

FIG. 27. Comparisons of film thickness between theoretical and experimental results before optimization. The average deviation is about 10.5%.

variation of the film thickness over time for the optimized textured thrust disk under different rotational speeds.

As illustrated in Fig. 28, at the same rotational speeds, the measured film thicknesses of the optimized textured thrust disk are generally higher than those of the initial design. Specifically, when the rotational speeds are 400, 1000, and 2000 rpm, the film thicknesses are increased by 5.26%, 5.98%, and 5.21%, respectively. These results indicate that, under the same speed and film thickness, the optimized thrust disk could generate greater load capacity.

Meanwhile, the theoretical water film thickness under the same load and rotational speed conditions was calculated using the AFML-RE method through iterative computation. A comparison between the experimental and theoretical results is also shown in Fig. 29. According to the results, the deviation between the theoretical and test results is approximately 10.18% at rotary speed of 400 rpm. The maximum deviation occurs at 2000 rpm, reaching about 12%. Considering high-speed vibration, manufacturing, and measurement errors, the theoretical predictions could be regarded to be in good agreement with the experimental data.

VII. LIMITATIONS AND FUTURE WORK

(1) In this study, the flow factor prediction model was developed based on a dataset constructed within the parameter ranges relevant to the current research. In the future work, the parameter range can be gradually expanded to establish a publicly accessible flow factor dataset, which would facilitate broader application and generalization of the proposed model.

(2) From an experimental perspective, due to constraints in funding and test conditions, the maximum achievable speed in this study was limited to 2000 rpm. When the speed increases above 2000 rpm, vibrations become significantly apparent. In the future, the manufacturing precision could be improved and a more stable motor could be used.

(3) Although recent studies have applied physics-informed neural networks (PINNs) to model the lubrication characteristics of smooth hydrodynamic bearings,[29,30] their application to textured surfaces remains largely unexplored. In our preliminary investigation, PINNs were found to perform well for smooth geometries but tended to lose critical localized information when applied to micro-textured bearings. PINNs tend to capture low-frequency (smooth) solutions well but perform poorly with high-frequency responses.[31] Nevertheless, as PINN methodologies continue to evolve, future work may explore

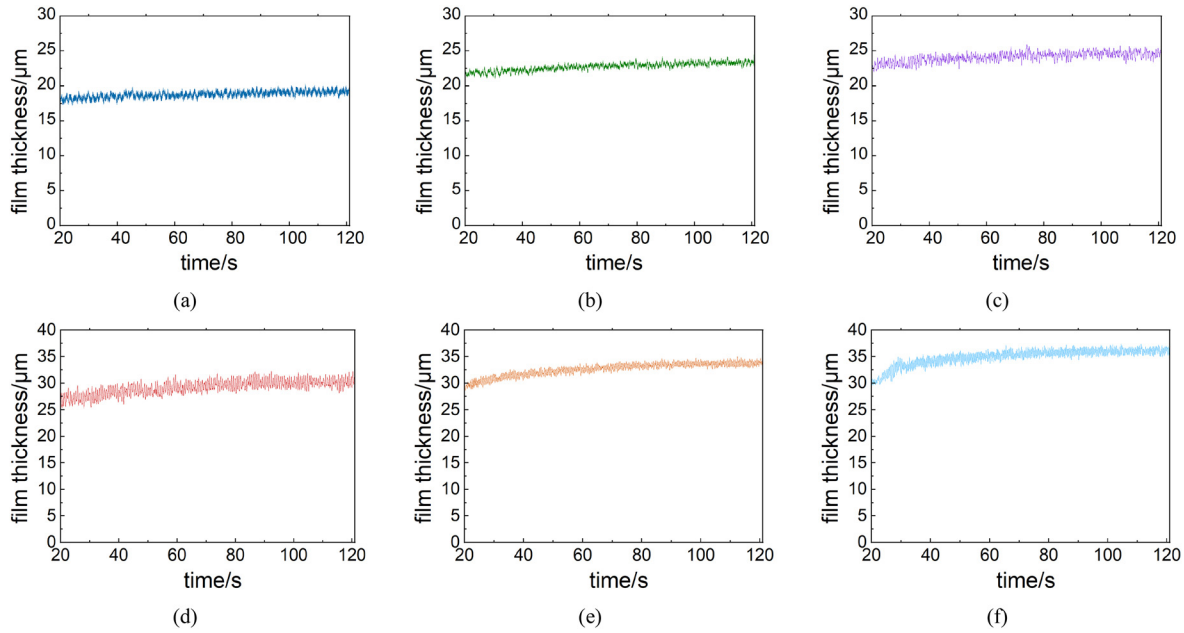

FIG. 28. Tested film thickness with different rotary speed after optimization. (a) 400 rpm, (b) 600 rpm, (c) 800 rpm, (d) 1000 rpm, (e) 1500 rpm, and (f) 2000 rpm. The optimized pad exhibits larger film thickness.

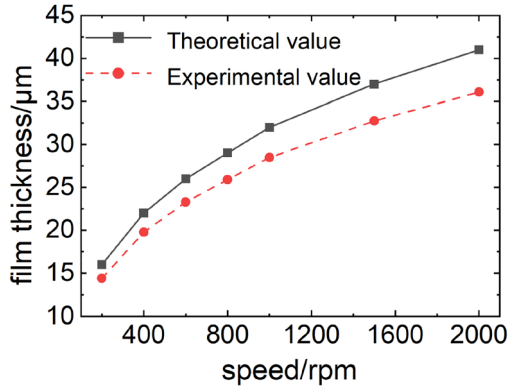

FIG. 29. Comparisons of film thickness between theoretical and experimental results after optimization. Deviations remain within 12%.

improved network structures or hybrid approaches to improve their applicability to textured lubrication problems.

VIII. CONCLUSIONS

This study addresses the conflicting challenges of computational efficiency and accuracy in the available numerical methods for lubrication characteristics of micro-textured bearings as well as their limited capability for cross-scale coupling. A novel AFML-ARE model was proposed, which integrates machine learning with the average flow model and the Reynolds equation. Flow factor prediction models were established using machine learning algorithms; the AFML-ARE model was developed by integrating the constructed flow factor prediction models with the averaged Reynolds equation; furthermore, particle swarm optimization was employed to perform texture parameter optimization. The main conclusions are summarized as follows:

(1) The flow factor prediction models based on Gaussian process regression achieved an average MAE of 0.008 825, an average MSE of 1.011×10^{-4}, and an average R^2 of 0.9984, demonstrating excellent prediction performance.
(2) The proposed AFML-ARE method significantly reduces computational time and improves efficiency for the textured bearing with high-density and micro-textures.
(3) Experimental results indicate that the theoretical film thickness of the thrust bearing are in good agreement with the experimental results, with an average error of 10.84%, verifying the accuracy and reliability of the theoretical model.

The proposed AFML-ARE cross-scale numerical method could provide a novel approach to overcoming existing research bottlenecks and enables efficient analysis bridging microscopic texture effects and macroscopic bearing performance

ACKNOWLEDGMENTS

This work was supported by the National Natural Science Foundation of China (Grant Nos. 51705131, 12172088, and 51635004) and the Postgraduate Research & Practice Innovation Program of Jiangsu Province (Grant No. KYCX25_0907).

AUTHOR DECLARATIONS

Conflict of Interest

The authors have no conflicts to disclose.

Author Contributions

Huihui Feng: Conceptualization (equal); Data curation (equal); Funding acquisition (equal); Investigation (equal); Methodology (equal); Project administration (equal); Supervision (equal); Writing – original draft (equal); Writing – review & editing (equal). **Xinyu Li:** Formal analysis (lead); Investigation (equal); Methodology (equal); Validation (equal); Visualization (equal); Writing – original draft (equal); Writing – review & editing (equal). **Shuyun Jiang:** Funding acquisition (equal); Project administration (equal); Supervision (equal); Writing – original draft (equal); Writing – review & editing (equal). **Ron van Ostayen:** Conceptualization (equal); Methodology (equal); Supervision (equal); Writing – original draft (equal). **Taohui Ji:** Formal analysis (equal); Validation (equal); Writing – original draft (equal).

DATA AVAILABILITY

The data that support the findings of this study are available within the article.

NOMENCLATURE

C	Film thickness at the maximum clearance of the thrust pad
D	Texture diameter
H	Film thickness
h_d	Film thickness increase caused by texture
h_{nom}	Nominal film thickness
h_0	Actual film thickness at a certain point
h_2	Film thickness at the maximum gap
L	Outer radius of the thrust pad
l_r	Length of equal spacing along the radial direction
N	Texture number
p	Pressure
p_0	Reference pressure
r_1	Inner radius of the thrust pad
r_2	Outer radius of the thrust pad
$ratioh$	The ratio of minimum film thickness h_1 to maximum film thickness h_2
U	Velocity
U_x	Velocity of textured bearing along the x-direction
U_y	Velocity of textured bearing along the y-direction
U_0	Characteristic velocity
α	Texture distribution angle with equal spacing
μ	Viscosity of fluid
μ_0	Dynamic viscosity of water
ϕ_{px}	Pressure flow factor in the x-direction
ϕ_{py}	Pressure flow factor in the y-direction
ϕ_{sx}	Shear flow factors in the x-direction
ϕ_{sy}	Shear flow factors in the y-direction

REFERENCES

[1]W. Litwin, "Marine propeller shaft bearings under low-speed conditions: Water vs. oil lubrication," Tribol. Trans. **62**(5), 839–849 (2019).
[2]A. Shinkarenko, Y. Kligerman, and I. Etsion, "The effect of surface texturing in soft elasto-hydrodynamic lubrication," Tribol. Int. **42**(2), 284–292 (2009).
[3]Z. Xie, J. Li, Y. Tian, P. Du, B. Zhao, and F. Xu, "Theoretical and experimental study on influences of surface texture on lubrication performance of a novel bearing," Tribol. Int. **193**, 109351 (2024).
[4]Y. A. Masmoudi, A. B. Chaouche, and A. Mokhtari, "Effect of rectangular rough dimples of textured surface on tribological behavior of a hydrodynamic journal bearing," Tribol. Int. **189**, 108945 (2023).
[5]H. Du, H. Li, and G. Meng, "Research on the reciprocating load characteristics of a hydrodynamic bearing surface with sloped grooves," Tribol. Int. **165**, 107282 (2022).
[6]D. Gropper, L. Wang, and T. J. Harvey, "Hydrodynamic lubrication of textured surfaces: A review of modeling techniques and key findings," Tribol. Int. **94**, 509–529 (2016).
[7]W. Wang, Y. He, J. Zhao, J. Mao, Y. Hu, and J. Luo, "Optimization of groove texture profile to improve hydrodynamic lubrication performance: Theory and experiments," Friction **8**(1), 83–94 (2020).
[8]S. Jiang, Q. Liu, J. Wang, H. Ji, and G. Dong, "Numerical optimization of asymmetric surface texturing under reciprocating sliding conditions," Tribol. Int. **180**, 108310 (2023).
[9]P. Li, F. Zhang, H. Zhang, T. Wang, Q. Wang, and W. Qiao, "Lubrication performance of kite-shaped microtexture under hydrodynamic lubrication," Tribol. Int. **179**, 108144 (2023).
[10]H. Feng and L. Peng, "Numerical analysis of water-lubricated thrust bearing with groove texture considering turbulence and cavitation," Ind. Lubr. Tribol. **70**(6), 1127–1136 (2018).
[11]F. J. Profito, S. C. Vladescu, T. Reddyhoff, and D. Dini, "Numerical and experimental investigation of textured journal bearings for friction reduction," Tribol. Int. **195**, 109643 (2024).
[12]L. Xue, Z. Yan, Y. Jiang, and T. Sun, "Influences of sharkskin texture on lubrication performance of elastic bearing friction pairs," Tribol. Lett. **72**(3), 103 (2024).
[13]L. Wang, Z. Han, G. Chen, and H. Su, "Thermo-hydrodynamic analysis of large-eccentricity hydrodynamic bearings with texture on journal surface," Proc. Inst. Mech. Eng., Part C **232**(19), 3564–3569 (2018).
[14]M. Chalkiopoulos, A. Charitopoulos, M. Fillon, and C. I. Papadopoulos, "Effects of thermal and mechanical deformations on textured thrust bearings optimally designed by a THD calculation method," Tribol. Int. **148**, 106303 (2020).
[15]Z. Xie, Y. Zhang, J. Zhou, and W. Zhu, "Theoretical and experimental research on the micro interface lubrication regime of water lubricated bearing," Mech. Syst. Signal Process. **151**, 107422 (2021).
[16]M. Rom, F. König, S. Müller, and G. Jacobs, "Why homogenization should be the averaging method of choice in hydrodynamic lubrication," Appl. Eng. Sci. **7**, 100055 (2021).
[17]A. De Kraker, R. A. J. Van Ostayen, and D. J. Rixen, "Development of a texture averaged Reynolds equation," Tribol. Int. **43**(11), 2100–2109 (2010).
[18]A. Waseem, İ. Temizer, J. Kato, and K. Terada, "Micro-texture design and optimization in hydrodynamic lubrication via two-scale analysis," Struct. Multidiscip. Optim. **56**(2), 227–248 (2017).
[19]M. Rom and S. Müller, "A reduced basis method for the homogenized reynolds equation applied to textured surfaces," Commun. Comput. Phys. **24**(2), 481–509 (2018).
[20]H. T. Yau, P. H. Kuo, and S. W. Hong, "Milling wear prediction using an artificial neural network model," Eng. Appl. Artif. Intell. **135**, 108686 (2024).
[21]M. G. Albayrak, E. Evin, O. Yiğit, M. Toğaçar, and B. Ergen, "Experimental and artificial intelligence approaches to measuring the wear behavior of DIN St28 steel boronized by the box boronizing method using a mechanically alloyed powder source," Eng. Appl. Artif. Intell. **120**, 105910 (2023).
[22]S. Han, G. Orzechowski, J. G. Kim, and A. Mikkola, "Data-driven friction force prediction model for hydraulic actuators using deep neural networks," Mech. Mach. Theory **192**, 105545 (2024).
[23]G. Cheng, C. Xiang, F. Guo, X. Wen, and X. Jia, "Prediction of the tribological properties of a polymer surface in a wide temperature range using machine learning algorithm based on friction noise," Tribol. Int. **180**, 108213 (2023).
[24]F. Aydin, R. Durgut, M. Mustu, and B. Demir, "Prediction of wear performance of ZK60/CeO_2 composites using machine learning models," Tribol. Int. **177**, 107945 (2023).
[25]J. Chen, C. Yu, Q. Cheng, Y. Guan, Q. Zhang, W. Li *et al.*, "Research on friction performance and wear rate prediction of high-speed train brake pads," Wear **514–515**, 204564 (2023).

[26]N. Patir and H. S. Cheng, "An average flow model for determining effects of three-dimensional roughness on partial hydrodynamic lubrication," J. Lubr. Technol. **100**(1), 12–17 (1978).
[27]H. Jiang, "Global convergence analysis of the generalized Newton and Gauss-Newton methods of the Fischer-Burmeister equation for the complementarity problem," Math. Oper. Res. **24**(3), 529–543 (1999).
[28]D. Bhaduri, P. Penchev, S. Dimov, and S. L. Soo, "An investigation of accuracy, repeatability and reproducibility of laser micromachining systems," Measurement **88**, 248–261 (2016).
[29]Y. Zhao, L. Guo, and P. P. L. Wong, "Application of physics-informed neural network in the analysis of hydrodynamic lubrication," Friction **11**(7), 1253–1264 (2023).
[30]D. J. Ramos, B. Z. Cunha, and G. B. Daniel, "Evaluation of physics-informed neural networks (PINN) in the solution of the Reynolds equation," J. Braz. Soc. Mech. Sci. **45**(11), 568 (2023).
[31]Y. Tang, L. Huang, L. Wu, and X. Meng, "Simulation of lubrication on rough surfaces with multiscale lubrication neural networks," Sci. China Technol. Sci. **68**, 1320303 (2025).